Featured in Physics

Ab initio ultrafast spin dynamics in solids

Junqing Xu, Adela Habib, Ravishankar Sundararaman, and Yuan Ping, and Yuan Ping, Department of Chemistry and Biochemistry, University of California, Santa Cruz, California 95064, USA
Department of Physics, Applied Physics and Astronomy, Rensselaer Polytechnic Institute, 110 8th Street, Troy, New York 12180, USA
Department of Materials Science and Engineering, Rensselaer Polytechnic Institute, 110 8th Street, Troy, New York 12180, USA



(Received 6 January 2021; accepted 7 October 2021; published 17 November 2021)

Spin relaxation and decoherence is at the heart of spintronics and spin-based quantum information science. Currently, theoretical approaches that can accurately predict spin relaxation of general solids including necessary scattering pathways and are capable of nanosecond to millisecond simulation time are urgently needed. We present a first-principles real-time density-matrix approach based on Lindblad dynamics to simulate ultrafast spin dynamics for general solid-state systems. Through the complete first-principles descriptions of pump, probe, and scattering processes including electron-phonon, electron-impurity, and electron-electron scatterings with self-consistent electronic spin-orbit couplings, our method can directly simulate the ultrafast pump-probe measurements for coupled spin and electron dynamics over nanoseconds at any temperatures and doping levels. We first apply this method to a prototypical system GaAs and obtain excellent agreement with experiments. We found that the relative contributions of different scattering mechanisms and phonon modes differ considerably between spin and carrier relaxation processes. In sharp contrast to previous work based on model Hamiltonians, we point out that the electron-electron scattering is negligible at room temperature but becomes dominant at low temperatures for spin relaxation in n-type GaAs. We further examine ultrafast dynamics in novel spin-valleytronic materials: monolayer and bilayer WSe2 with realistic defects. We find that spin relaxation is highly sensitive to local symmetry and chemical bonds around defects. For the bilayer WSe2, we identify the scattering pathways in ultrafast dynamics and determine relevant dynamical properties, essential to its utilization of unique spin-valley-layer locking effects. Our work provides a predictive computational platform for spin dynamics in solids, which has potential for designing new materials ideal for spintronics and quantum information technology.

DOI: 10.1103/PhysRevB.104.184418

I. INTRODUCTION

Spin is a fundamental quantum mechanical property of electrons and other particles. The spin states can be used as the basis of quantum bits in quantum information science (QIS) [1], in addition to being used in spintronics, analogous to electrical charge in conventional electronics [2]. The key property for spintronics and spin-based QIS is the lifetime of spin states. Stable manipulations of spin states in practical applications require lifetimes on the order of hundreds of nanoseconds or even milliseconds. Determining the underlying mechanisms and controlling spin relaxation are vital to reach long spin lifetimes at room temperature. Experimentally spin relaxation can be studied through ultrafast magneto-optical pump-probe [3,4] and spin transport measurements [5], allowing the direct observations of dynamical processes and quantitative determination of spin relaxation time, τ_s .

Despite significant experimental progress and several proposed systems in the past decades [2,6], materials with properties required for practical QIS and spintronics appli-

cations such as long τ_s at room temperature remain to be found [1,5,7]. Theoretical predictions of materials properties have been mostly focused on electronic excitations [8–10] and electron-hole recombinations [11–13] of potential spin defects for QIS applications. Reliable prediction of spin lifetime and dominant relaxation mechanisms will allow rational design of materials in order to accelerate the identification of ideal materials for quantum technologies, while forgoing the need for experimental search over a large number of materials.

Until recently, most state-of-the-art theoretical methods to study spin dynamics of solid-state materials have been limited to simplified and system-specific models that require prior input parameters [2,14–16]. These methods laid an important theoretical foundation for spin dynamics, such as the spin-Bloch kinetic equations developed from nonequilibrium Green's function theory (NEGFT) [17]. Reference [18] derived a closed equation of motion for the electronic single-particle density matrix, including different scattering matrices, which may be applicable to spin dynamics. However, because of the simplified electronic structure and electron-phonon coupling matrices, quantitative prediction of spin relaxation remains out of reach. Occasionally, even trends in τ_s predicted by such models may be incorrect as shown recently for graphene [19]. Furthermore, these models are

^{*}These authors contributed equally to this work.

[†]sundar@rpi.edu

[‡]yuanping@ucsc.edu

unable to provide predictive values for new materials where prior inputs are not available.

Prior to our work, the existing first-principles methodology for spin lifetime has been mostly based on spin-flip matrix elements in a specialized Fermi's Golden Rule [20–22], which is only applicable to systems with Kramers's degeneracy or spatial inversion symmetry and not suitable for lots of materials promising for quantum computing and spintronics applications [2,5]. Other first-principles techniques like realtime time-dependent density functional theory (TDDFT) [23] are challenging for crystalline systems due to the high computational cost for describing phonon relaxations that require large supercells. More importantly, the long simulation time over nanoseconds often required by spin relaxation is a major difficulty for TDDFT, which is only practical for tens to a few hundreds of femtoseconds. While spin dynamics based on TDDFT has been recently performed for ultrafast demagnetization of magnetic systems within tens of femtoseconds [24–26], the intrinsic time scale and supercell limitations mentioned above remain.

We recently derived a generalized rate equation [27] based on a first-principles density matrix (DM) Lindblad dynamics framework, which provides accurate spin relaxation time due to spin-orbit and electron-phonon couplings for a broad range of materials, with arbitrary symmetry. However, our previous work requires that the system is already in a quasiequilibrium state when the dynamics can be described by a singleexponential decay, which cannot describe coupled spin and carrier dynamics at an out-of-equilibrium state in ultrafast pump-probe experiments. In this work, we develop a realtime ab initio DM dynamics method based on this theoretical framework, with complete descriptions of scattering processes, including electron-phonon (e-ph), electron-impurity (e-i), and electron-electron (e-e) scattering processes, being adequate for over nanoseconds to milliseconds simulation time. Specifically, compared to the generalized rate equation in our previous work, DM dynamics with explicit real-time evolutions allow coupled carrier and spin relaxation away from quasiequilibrium with all decoherence pathways simultaneously. This will facilitate direct prediction of experimental signatures in ultrafast magneto-optical spectroscopy to unambiguously interpret experimental probes of spin and electron dynamics.

We will demonstrate the generality of our approach by considering two prototypical and disparate systems, GaAs and few-layer WSe₂, which have very different spin relaxation mechanisms.

We will first apply our DM dynamics methodology to investigate the ultrafast spin dynamics of GaAs, which has gained broad interest in spintronics over past decades [2,28–31] and more recently [32–34], partly due to its long spin lifetime especially in the *n*-doped material at relatively low temperature [28]. Despite various experimental [28,29,35–37] and theoretical [2,30,31,38–40] (mostly using a parametrized model Hamiltonian) studies previously, the dominant spin relaxation mechanism of bulk GaAs under various temperatures and doping levels remains unclear. For example, References [30,39] claimed *e*-i and *e*-ph scatterings dominate spin relaxation at low and room temperatures, respectively; however, Refs. [31,40] conclude that *e-e* scattering may be more

important at room temperature and even more at lower temperatures. Moreover, electron-phonon scattering matrices, which can be accurately obtained from first principles, are very difficult to be precisely described in the parametrized models used previously. Most importantly, the applicability of the empirical Dyakonov-Perel (DP) relation, which is widely used for describing inversion-asymmetric systems including GaAs, needs to be carefully examined. Throughout this work, we provide complete and unambiguous insights on the underlying mechanism of spin relaxation and applicability of the DP relation for GaAs from first-principles DM dynamics.

Due to broken inversion symmetry and strong spin-orbit coupling (SOC), monolayer transition metal dichalcogenides (TMDs) exhibit exciting physical properties including valley-specific optical excitation and spin-valley locking effects. In Refs. [41,42], it was shown that by introducing doping in monolayer TMDs, ultraslow decays of Kerr rotations, which correspond to ultralong spin and valley lifetimes of resident carriers especially resident holes can be observed at low temperatures. Those features make monolayer TMDs advantageous for spin-valleytronics and (quantum) information processing.

Besides monolayers, bilayer TMDs recovering inversion symmetry have also attracted significant interest because of the new "layer" degree of freedom or layer pseudospin in addition to spin and valley pseudospin [43–45]. Previous studies already concluded that electronic states at K/K' valleys of a bilayer TMD are approximately a superposition of those of two monolayers. This allows us to tune which layer carriers and/or spins are localized by a perpendicular electric field E_z , and make use of the spin-valley-layer locking effects for spin-valleytronic applications.

Although spin-valley relaxation of resident carriers in monolayer TMDs, which is most relevant to spin-valleytronic applications, has been extensively examined [27,41,42,46], the underlying dynamics especially the effects of different types of impurities have not been investigated through predictive *ab initio* simulations. Furthermore, for bilayer TMDs, the study on spin-valley dynamics is still in its infancy with few ultrafast measurements which however do not exhibit long spin relaxation time and are lacking spin-valley-layer locking properties [47–49]. There is a lack of knowledge of the role of scattering processes and the scattering pathways for spin-valley dynamics of free carriers in bilayers, which prevents researchers from realizing and manipulating spin-valley-layer locking effects for designing spin-valleytronic devices.

In this work, we will answer the above questions by performing *ab initio* real-time dynamics simulations with a circularly polarized pump pulse and relevant scattering mechanisms. We focus on WSe₂ due to its larger valence band SOC splitting and focus on dynamics of holes since τ_s of holes seem longer than electrons.

In the following, we first introduce our theoretical formalism of the real-time density-matrix approach with various scattering processes and pump-probe spectroscopy. In particular, we focus on spin-orbit-mediated spin relaxation and decoherence processes under the existence of electron scatterings, which are rather common in semiconductors and metals [2,17]. We use this method to simulate pump-probe Kerr rotation and real-time spin dynamics, by using GaAs as a

prototypical example and comparing with experiments. Next, we study spin lifetime dependence on the temperature and doping level, where the dominant mechanisms can vary significantly. We then discuss the roles of different scattering mechanisms and phonon modes in carrier and spin relaxations, respectively, in order to resolve related long-standing controversies. We further simulate ultrafast dynamics in monolayer and bilayer WSe₂ and extract useful dynamical properties. Our work provides predictive theory and a computational platform for open quantum dynamics, and offers critical insights for spin relaxation and decoherence in general solid-state systems.

II. THEORY

A. Real-time density-matrix dynamics and spin relaxation time

To provide a general formulation of quantum dynamics in solid-state materials, we start from the Liouville-von Neumann equation in the interaction picture,

$$\frac{d\rho(t)}{dt} = -i[H'(t), \rho(t)],\tag{1}$$

$$H'(t) = H(t) - H_0(t),$$
 (2)

where H, H_0 , and H' are the total, unperturbed, and perturbed Hamiltonian, respectively. In this work, the total Hamiltonian is

$$H = H_0 + H_{\text{pump}} + H_{e-i} + H_{e-ph} + H_{e-e},$$
 (3)

$$H_0 = H_{e,0} + H_{\text{efield}} + H_z + H_{\text{ph}},$$
 (4)

where $H_{e,0}$ is electronic Hamiltonian under zero external field. In this work, H_{efield} is the Hamiltonian induced by a perpendicular electric field E_z along the vacuum direction. H_z is the Zeeman Hamiltonian corresponding to an external magnetic field \mathbf{B} , $H_z = g_s \mu_B \mathbf{B} \cdot \mathbf{s}$, where $\mathbf{s} = (s_x, s_y, s_z)$ and s_i is the spin matrix in Bloch basis under zero field. g_s is the g factor and μ_B is the Bohr magneton. H_{pump} is the Hamiltonian of the pump pulse and will be described below. H_{ph} is the phonon Hamiltonian, while H_{e-i} , $H_{e-\text{ph}}$, and H_{e-e} describe the electronimpurity, electron-phonon, and electron-electron interactions, respectively. The detailed forms of the interaction Hamiltonians are given in Appendix \mathbf{A} .

In practice, the many-body density matrix master equation in Eq. (1) is reduced to a single-particle one and the environmental degrees of freedom are traced out [50]. The total rate of change of the density matrix is separated into terms related to different parts of Hamiltonian,

$$\frac{d\rho}{dt} = \frac{d\rho}{dt}\bigg|_{\text{coh}} + \frac{d\rho}{dt}\bigg|_{\text{scatt}},\tag{5}$$

where ρ is the density matrix of electrons. Above, $\frac{d\rho}{dt}|_{\text{coh}}$ describes the coherent dynamics of electrons under potentials or fields, e.g., the applied pump pulse, while $\frac{d\rho}{dt}|_{\text{scatt}}$ captures the scattering between electrons and other particles.

To obtain Eq. (5), which involves only the dynamics of electrons or the electronic subsystem, we have assumed the environmental subsystem is not perturbed by the change of the electronic subsystem, which in this work means there is no dynamics of phonons. This assumption is valid when the

system is not far from equilibrium, e.g., when excitation is weak. In most spin dynamics experiments, it is desirable to work in the low excitation density limit to avoid additional complexities and focus on the physics of spin dynamics. Indeed in many experiments, e.g., in Refs. [28,51], pump fluence and excitation density are controlled to be low, e.g., excitation density 2×10^{14} cm⁻² for GaAs. Therefore, phonon dynamics can be safely excluded in the current stage. The inclusion of phonon degrees of freedom in the density-matrix dynamics has been discussed in detail in Refs. [50,52] with a model Hamiltonian, which can be our future work to implement from first principles.

To define spin lifetime, we follow the time evolution of the observable

$$S_i = \text{Tr}(s_i \rho),$$
 (6)

where s_i is the spin operator (i = x, y, z). This time evolution must start at an initial state (at $t = t_0$) with a net spin, i.e., $\delta \rho(t_0) = \rho(t_0) - \rho^{\rm eq} \neq 0$ such that $\delta S_i(t_0) = S_i(t_0) - S_i^{\rm eq} \neq 0$, where "eq" corresponds to the final equilibrium state. We evolve the density matrix through Eq. (5) using an adaptive Runge-Kutta fourth-order method for a long enough simulation time, typically from tens of picoseconds to several nanoseconds, until the evolution of $S_i(t)$ can be reliably fitted by

$$S_{i}(t) - S_{i}^{\text{eq}} = \left[S_{i}(t_{0}) - S_{i}^{\text{eq}} \right] \exp \left[-\frac{t - t_{0}}{\tau_{s,i}} \right]$$

$$\times \cos[\omega_{B}(t - t_{0}) + \phi]$$
(7)

to extract the relaxation time, $\tau_{s,i}$. Above, ω_B is the oscillation frequency due to energy splitting in general, which under an applied magnetic field **B** would include a contribution $\approx 0.5g_s\mu_B(\mathbf{B}\times\hat{\mathbf{S}}_i)$.

In order to examine whether the spin relaxation time depends on how the spin imbalance is generated, we implement two general ways to initialize $\delta\rho(t_0)$. First, for simulating pump-probe experiments, we choose $\delta\rho(t_0)$ corresponding to interaction with a pump pulse. Second, we use the technique proposed previously in Ref. [27] by applying a test magnetic field at $t=-\infty$, allowing the system to equilibrate with a net spin and then turning it off suddenly at t_0 .

B. Scattering terms

The scattering part of the master equation can be separated into contributions from several scattering channels,

$$\left. \frac{d\rho}{dt} \right|_{\text{scatt}} = \sum_{c} \frac{d\rho}{dt} \bigg|_{c},\tag{8}$$

where c labels a scattering channel. Under the Born-Markov approximation, in general we have [18]

$$\left. \frac{d\rho_{12}}{dt} \right|_{c} = \frac{1}{2} \sum_{345} \left[\frac{(I - \rho)_{13} P_{32,45}^{c} \rho_{45}}{-(I - \rho)_{45} P_{45,13}^{c,*} \rho_{32}} \right] + \text{H.c.}, \quad (9)$$

where P^c is the generalized scattering-rate matrix and H.c. is Hermitian conjugate. The subindex, e.g., "1", is the combined index of k-point and band. The weights of k points must be considered when doing a sum over k points. Note that P^c

in the interaction picture is related to its value $P^{S,c}$ in the Schrodinger picture as

$$P_{1234}^{c}(t) = P_{1234}^{S,c} \exp[i(\epsilon_1 - \epsilon_2 - \epsilon_3 + \epsilon_4)t], \qquad (10)$$

where ϵ_i are single-particle eigenvalues of H_0 . Below, we consider three separate scattering mechanisms—electron-impurity (e-i), electron-phonon (e-ph), and electron-electron (e-e)—and describe the matrix elements for each.

For electron-phonon scattering, the scattering matrix is given by [18]

$$P_{1234}^{\text{S,e-ph}} = \sum_{q\lambda+} A_{13}^{q\lambda\pm} A_{24}^{q\lambda\pm,*},\tag{11}$$

$$A_{13}^{q\lambda\pm} = \sqrt{\frac{2\pi}{\hbar}} g_{12}^{q\lambda\pm} \sqrt{\delta_{\sigma}^{G}(\epsilon_{1} - \epsilon_{2} \pm \omega_{q\lambda})} \sqrt{n_{q\lambda}^{\pm}}, \tag{12}$$

where q and λ are the phonon wave vector and mode, $g^{q\lambda\pm}$ is the electron-phonon matrix element, resulting from the absorption (–) or emission (+) of a phonon, computed with self-consistent spin-orbit coupling from first principles [53], $n_{q\lambda}^{\pm} = n_{q\lambda} + 0.5 \pm 0.5$ in terms of phonon Bose factors $n_{q\lambda}$, and δ_{σ}^{G} represents an energy-conserving δ function broadened to a Gaussian of width σ .

Next, for electron-impurity scattering, the scattering matrix is given by

$$P_{1234}^{S,e-i} = A_{13}^i A_{24}^{i,*}, (13)$$

$$A_{13}^{i} = \sqrt{\frac{2\pi}{\hbar}} g_{13}^{i} \sqrt{\delta_{\sigma}^{G}(\epsilon_{1} - \epsilon_{3})} \sqrt{n_{i} V_{\text{cell}}}, \tag{14}$$

$$g_{13}^i = \langle 1|V^i|3\rangle,\tag{15}$$

where n_i and V_{cell} are impurity density and unit cell volume, respectively, and V^i is the impurity potential. In this work, we deal with ionized and neutral impurities differently. For ionized impurities, V^i is proportional to the screened Coulomb potential [54]; for neutral impurities, we compute impurity potentials with supercell methods from DFT (see Appendix A for further details).

Finally, for electron-electron scattering, the scattering matrix is given by [18]

$$P_{12,34}^{8,e-e} = 2\sum_{56,78} (I - \rho)_{65} \mathcal{A}_{15,37} \mathcal{A}_{26,48}^* \rho_{78}, \tag{16}$$

$$\mathcal{A}_{1234} = \frac{1}{2} (A_{1234} - A_{1243}),\tag{17}$$

$$A_{1234} = \frac{1}{2} \sqrt{\frac{2\pi}{\hbar}} \left[g_{1234}^{e-e} (\delta_{\sigma,1234}^G)^{1/2} + g_{2143}^{e-e} (\delta_{\sigma,2143}^G)^{1/2} \right], \quad (18)$$

$$g_{1234}^{e-e} = \langle 1(r)|\langle 2(r')|V(r-r')|3(r)\rangle|4(r')\rangle,$$
 (19)

where V(r-r') is the screened Coulomb potential and $\delta_{\sigma,1234}^G = \delta_{\sigma}^G(\epsilon_1 + \epsilon_2 - \epsilon_3 - \epsilon_4)$ is a Gaussian-broadened energy conservation function. The screening is described by a random-phase-approximation (RPA) dielectric function (details in Appendix A). Although the above equations describe all possible scattering processes between electrons and holes, we only consider those between conduction electrons here, which are appropriate for *n*-type Group III–V semiconductors [30,39]. The electron-hole scattering can be important for intrinsic and *p*-type material [30,39]. We note that unlike the

e-ph and e-i channels, $P^{S,e-e}$ (as well as the dielectric screening in V) is a function of ρ and needs to be updated during time evolution of ρ . This is a clear consequence of the two-particle nature of e-e scattering. $P^{S,e-e}$ can be written as the difference between a direct term and an exchange term,

$$P^{S,e-e} = P^{S,e-e,d} - P^{S,e-e,x},$$
 (20)

$$P^{S,e-e,d} = \sum_{56,78} (I - \rho)_{65} A_{15,37} A_{26,48}^* \rho_{78}, \tag{21}$$

$$P^{\text{S,e-e,x}} = \sum_{56.78} (I - \rho)_{65} A_{15,37} A_{26,84}^* \rho_{78}. \tag{22}$$

According to Ref. [50], the direct term is expected to dominate the dynamical scattering processes between conduction or valence electrons, allowing us to neglect the exchange term here.

C. Pump-probe simulation

In the nonrelativistic limit, the light-matter interaction Hamiltonian operator (\widehat{H}_{e-p}) reads [55]

$$\widehat{H}_{e-p} = \frac{e}{m_e} \mathbf{A}(t) \cdot \widehat{\mathbf{p}} + \frac{e}{2m_e} \mathbf{A}(t) \cdot \mathbf{A}(t) + g_e \mu_B \widehat{\mathbf{s}} \cdot (\nabla \times \mathbf{A}(t)),$$

where $\mathbf{A}(t)$ is the vector potential and $\mathbf{A}(t) = \mathbf{A}_0(t)e^{-i\omega t} + \mathbf{A}_0^*(t)e^{i\omega t}$ with $\mathbf{A}_0(t)$ being the complex amplitude and ω being photon frequency. $\widehat{\mathbf{p}}$ is the momentum operator. $g_e \approx 2.0023192$ is an anomalous gyromagnetic ratio. The second quadratic term plays a role only when pump fluence is higher by several orders of magnitude than that in usual spin dynamics experiments and can be safely neglected. Since $\nabla \times \mathbf{A}(t) = -i\mathbf{q}_{\text{photon}} \times \mathbf{A}(t)$ [55] and the photon wavevector $\mathbf{q}_{\text{photon}}$ is quite small (the photon wavelength is much longer than the scale of unit cells), the third term is also negligible. Therefore, we will only keep the first $\mathbf{A}(t) \cdot \widehat{\mathbf{p}}$ term.

The interaction with a pump pulse of frequency ω_{pump} in the interaction picture is given by

$$H_{\text{pump},k,mn}(\omega_{\text{pump}},t) = \frac{e}{m_e} \mathbf{A}_0(t) \cdot \mathbf{p}_{k,mn} e^{it(\epsilon_m - \epsilon_n - \omega_{\text{pump}})} + \text{H.c.},$$
(23)

where m, n represent the band indices and k represents the k-point sampling in the first Brillouin zone. For a Gaussian pulse centered at time t_{center} with width τ_{pump} ,

$$\mathbf{A}_0(t) = \mathbf{A}_0 \frac{1}{\sqrt{\sqrt{\pi} \tau_{\text{pump}}}} \exp\left[-(t - t_{\text{center}})^2 / \left(2\tau_{\text{pump}}^2\right)\right]. \quad (24)$$

Note that the corresponding pump fluence is $I_{\text{pump}} = \omega_{\text{pump}}^2 |A_0|^2 / (8\pi\alpha)$, where α is a fine structure constant. As a part of the coherent portion of the time evolution, the dynamics due to this term are captured directly in the Liouville form [56,57]:

$$\left. \frac{d\rho}{dt} \right|_{\text{pump}} = -i[H_{\text{pump}}, \rho].$$
 (25)

The probe pulse interacts with the material similarly to the pump pulse, and could be described in exactly the same way in principle. However, this would require repeating the simulation for several values of the pump-probe delay. Instead, since the probe is typically chosen to be of sufficiently low intensity, we use second-order time-dependent perturbation theory to capture its interaction with the system,

$$\Delta \rho^{\text{probe}} = \frac{1}{2} \sum_{345} \left\{ \begin{aligned} & [I - \rho(t)]_{13} P_{32,45}^{\text{probe}} \rho(t)_{45} \\ & - [I - \rho(t)]_{45} P_{45,13}^{\text{probe},*} \rho(t)_{32} \end{aligned} \right\} + \text{H.c.},$$
(26)

where P^{probe} is the generalized scattering-rate matrix for the probe in the interaction picture. Its corresponding Schrodinger-picture quantity is

$$P_{1234}^{\text{S,probe}} = \sum_{\pm} A_{13}^{\text{probe}, \pm} A_{24}^{\text{probe}, \pm, *},$$
 (27)

$$A_{13}^{\text{probe},\pm} = \sqrt{\frac{2\pi}{\hbar}} \frac{e}{m_e} (\mathbf{A}_0^{\text{probe}} \cdot \mathbf{p}) \sqrt{\delta_{\sigma}^G(\epsilon_1 - \epsilon_3 \pm \omega_{\text{probe}})}. (28)$$

The dielectric function change $\Delta\epsilon$ between the excited-state and ground-state absorption detected by the probe is then

$$\operatorname{Im}\Delta\epsilon = \frac{2\pi}{(\omega_{\text{probe}})^3 |A_0^{\text{probe}}|^2} \operatorname{Tr}(H_0 \Delta \rho^{\text{probe}}). \tag{29}$$

Note that $\Delta \rho^{\text{probe}}$ contains $|A_0^{\text{probe}}|^2$ so that $\text{Im}\Delta\epsilon$ is independent of A_0^{probe} . The above $\text{Im}\Delta\epsilon$ is a functional of the density matrix according to Eq. (26) and is an extension of the usual independent-particle $\text{Im}\epsilon$ depending on just occupation numbers [58]. After computing $\text{Im}\Delta\epsilon$ above, the real part $\text{Re}\Delta\epsilon$ can be obtained from the Kramers-Kronig relation.

By summing up the dielectric function change $\Delta \epsilon$ computed above with the dielectric function for ground-state absorption, we can obtain the excited-state ϵ as inputs for Kerr and Faraday rotation calculations [59]. These correspond to the rotations of the polarization plane of a linearly polarized light, reflected by (Kerr) and transmitted through (Faraday) the material, after a pump excitation with a circularly polarized light. Time-resolved Kerr rotation (TRKR) and time-resolved Faraday rotation (TRFR) have been widely used to study spin dynamics of materials [28,36]. In a TRKR experiment, a circularly polarized pump pulse is used to excite valence electrons of the sample to conduction bands. The transitions approximately satisfy the selection rule of $\Delta m_i =$ ± 1 for left and right circularly polarized pulses, respectively, where m_i is the secondary total angular momentum. TRKR works by measuring the changes of polarization of reflected light, which qualitatively is proportional to the small population imbalance of electronic states with different m_i .

Specifically, the Kerr rotation angle θ_K is computed with dielectric functions by

$$\theta_K = \operatorname{Im} \frac{\sqrt{\epsilon_+} - \sqrt{\epsilon_-}}{1 - \sqrt{\epsilon_+}\sqrt{\epsilon_-}},\tag{30}$$

where \pm denotes the left and right circular polarization, respectively.

III. COMPUTATIONAL DETAILS

The ground-state electronic structure, phonon, and *e*-ph matrix element calculations of GaAs and few-layer WSe₂ are

first calculated using density functional theory (DFT) with relatively coarse k and q meshes in the JDFTX plane-wave DFT code [60]. For GaAs, we use the experimental lattice constant of 5.653 Å [61], and select the SCAN exchangecorrelation functional [62] for an accurate description of the electron effective mass (see Sec. II in the Supplemental Material [63]; see also Refs. [64-66] therein). We also apply a scissor operator to the DFT values to reach an experimental band gap of 1.43 eV [67]. For WSe₂, we used the Perdew-Burke-Ernzerhof (PBE) exchange correlation functional along with the DFT-D2 pair potential dispersion corrections [68]. The resulting lattice constant is 3.32 Åand the distance between two W-atom planes is 6.419 Å, close to experimental values of bulk WSe₂, 3.297 and 6.491 Å [69]. The phonon calculations of GaAs and WSe₂ employ a $4 \times 4 \times 4$ and 6×6 supercell, respectively. We use optimized norm-conserving Vanderbilt (ONCV) pseudopotentials [70] with self-consistent spin-orbit coupling throughout, which we find converged at a plane-wave kinetic energy cutoff of 34 and 62 Ry for GaAs and WSe₂, respectively. With these computational parameters, we find the effective mass of conduction electrons of GaAs to be $0.054m_e$, close to the experimental value of $0.067m_e$ [67]. (More convergence tests can be found in the Supplemental Material (SM) [63]).

We then transform all quantities from the plane-wave basis to the maximally localized Wannier function basis [71], and interpolate them [53,72–76] to substantially finer k and q meshes. The Wannier interpolation approach fully accounts for polar terms in the e-ph matrix elements and phonon dispersion relations, using the approach developed by Verdi and Giustino [77] for three-dimensional (3D) and the methods in Refs. [78,79] for two-dimensional (2D) systems. The Born effective charges and dielectric constants are calculated from the open-source code QUANTUM ESPRESSO [80].

For GaAs, the fine k and q meshes are $288 \times 288 \times 288$ for simulations at 300 K and are finer at lower temperature, e.g., $792 \times 792 \times 792$ for simulations at 30 K. This is necessary to sample enough electronic states around band edges and for spin lifetime convergence within 20%. The k and q convergence are easier for WSe₂ due to much larger effective masses, and we used 168×168 and 600×600 meshes at 50 and 10 K, respectively. The computation of e-i and e-e matrix elements and the real-time dynamics simulations are done with a custom code interfaced to JDFTX. The energy-conservation smearing parameter σ is chosen to be comparable to or smaller than k_BT for each calculation. Detailed convergence tests of the number of k points and the energy window for electronic states at various smearing parameters can be found in the Supplemental Material [63].

IV. RESULTS AND DISCUSSIONS

A. Applications to *n*-doped GaAs

1. Spin dynamics and its relation to TRKR

In general, the time evolution of the Kerr rotation angle θ_K [see Eq. (30)] is not equivalent to that of spin along the direction of reflected light, and in fact, they can be quite different in some cases [41]. There are few first-principles studies of TRKR considering scattering processes in a form of

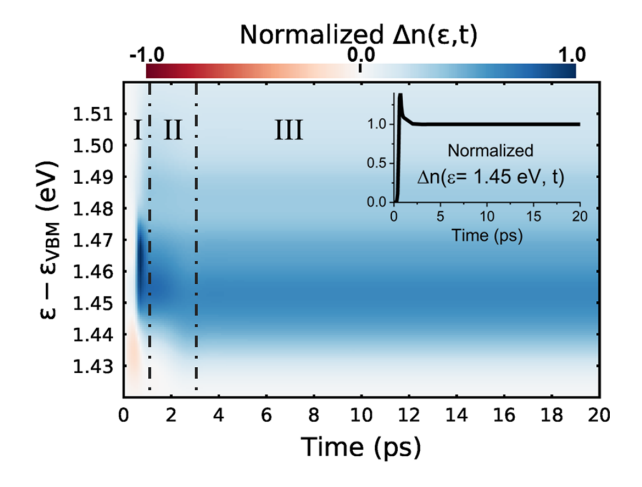
semiclassical Boltzmann equation [58]. A full quantum description of scatterings with a nondiagonal density matrix in TRKR has not been presented in previous first-principles studies, to the best of our knowledge. And the relation between dynamics of θ_K and spin observable for general systems including GaAs has not yet been well examined.

Using our density-matrix approach, we are able to directly simulate the nonequilibrium ultrafast dynamics of optically excited systems during which the dynamics of different electronic quantities such as spin and carriers can be strongly coupled. We include all scattering terms in a full quantum description as shown in the Sec. II B and Appendix A. We perform the real-time dynamics simulations of n-type GaAs for tens of picoseconds at room temperature and several nanoseconds at low temperature until the fitted spin lifetime does not change any more. Having temporal density matrix, we can further analyze the dynamics of various observables, including occupation, spin, and Kerr rotation angle easily. We then examine the relation between θ_K and spin in the dynamics.

Figure 1 shows the energy-resolved dynamics of carriers $\Delta n(\epsilon,t) = n(\epsilon,t) - n(\epsilon,0)$ and spins $S_z(\epsilon,t)$. The energy-resolved observable $O(\epsilon)$ is defined as $\text{Re}[\sum_{k,mn} o_{k,nm} \rho_{k,nm} \delta(\epsilon - \epsilon_{km})]$, where o is an operator matrix. We can see that during the first picosecond (region I in Fig. 1), both observables vary quickly due to the existence of the pump processes and both have their maximum at an energy slightly lower than the pump energy, 1.47 eV (slightly larger than the band gap, 1.43 eV), at a time shortly after the time center of the pump pulse, 0.5 ps. Interestingly, after the pump being not active or after 0.8–1 ps, carriers and spins simultaneously relax until 2–3 ps [region II in Figs. 1(a) and 1(b)]. Afterward [region III in Figs. 1(a) and 1(b)], carriers stay unchanged but spins $S_z(\epsilon,t)$ decay exponentially as shown in the insets of Figs. 1(a) and 1(b).

We have further analyzed the dynamics of Kerr rotation angle θ_K and compared it with spin dynamics. From Fig. 2(a), we can see that during pump processes and shortly after them (from 0 to 2 ps), $\theta_K(t)$ has strong oscillations and is sensitive to the probe energy ω_{probe} . The ω_{probe} sensitivity may be partly attributed to the energy dependence of carrier and spin dynamics. From Figs. 2(a) and 2(b), it can be seen that after 3 ps (or in time region III defined in Fig. 1), θ_K with different ω_{probe} decay exactly the same. We can also find that with a pump pulse, the relaxation time of the Kerr rotation is the same as that of S_z , i.e., $\tau_{s,z}$. Moreover, it turns out that $\tau_{s,z}$ does not depend on how spin imbalance is generated—by a circularly polarized pump pulse or by turning off a test magnetic field along the z direction (see Sec. II A). This may indicate that if the system is not extremely far from equilibrium, spin relaxation along direction i is not sensitive to the way of generating spin imbalance, as long as the degrees of freedom other than S_i are not relevant or disappear in a short time. According to these observations, hereinafter, we will do real-time dynamics starting from a $\delta \rho$ generated by turning off a test magnetic field and fit $\tau_{s,z}$ from time evolution of S_7 .

We have also studied the effects of ω_{pump} and pump fluence I_{pump} on spin relaxation of *n*-GaAs at 300 K. We find that ω_{pump} has very weak effects on spin relaxation



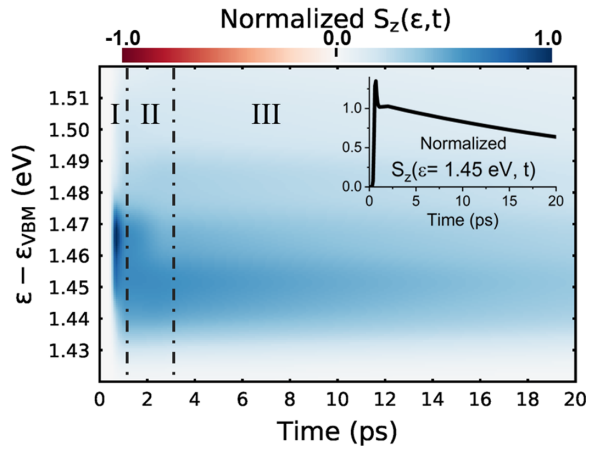


FIG. 1. The energy-resolved dynamics of carriers (a) $\Delta n(\epsilon,t) = n(\epsilon,t) - n(\epsilon,0)$ and (b) spins $S_z(\epsilon,t)$ of conduction electrons with a circularly polarized pump pulse centered at 0.5 ps. The insets on the top right of both panels show $\Delta n(\epsilon,t)$ and $S_z(\epsilon,t)$ at $\epsilon = 1.45$ eV. The pump energy $\omega_{\text{pump}} = 1.47$ eV is chosen to be higher than the band gap, 1.43 eV [67]. The width of the pump pulse τ_{pump} is 100 fs. The pump fluence I_{pump} is low at 0.01 μ J cm⁻². The dynamics can be approximately divided into three regions: regions I, II, and III labeled in this figure. In region I, the system is excited by a pump pulse. In region II, pump processes are already finished, then both carriers and spins relax simultaneously. In region III, the carrier distribution stays unchanged while spins keep decaying.

but $\tau_{s,z}$ decreases with pump fluence. See more details in Appendix C.

2. Temperature dependence of spin lifetime and its dominant relaxation mechanism

As discussed earlier, long-standing controversies remain for the dominant spin relaxation mechanism of GaAs at different temperature and doping level [30,31,39,40], which will be resolved in the following sections. We start from study $\tau_{s,z}$ of n-GaAs as a function of temperature at a moderate doping level (2 × 10¹⁶ cm⁻³). For simplicity, we assume all impurities are fully ionized, so that the impurity density n_i is equal to the free carrier density $n_{\rm free}$. We first compared our calculated spin lifetime with experimental results in Fig. 3. Our results of $\tau_{s,z}$ of n-GaAs give good agreement with experiments at various temperatures [28,36,37,81]. Different experiments have

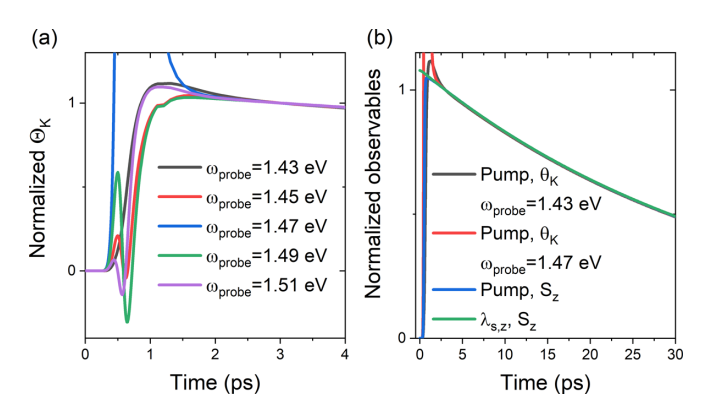


FIG. 2. (a) Compare the dynamics of Kerr rotation angle θ_K at different probe energies ω_{probe} excited by a circularly polarized pump pulse in the first few picoseconds. Fast oscillations in the first 2 ps are due to the pump pulse and coupled spin and carrier relaxation. (b) Compare relaxation of different observables: θ_K with different ω_{probe} (denoted by black and red lines) and S_z with initial spin imbalance generated by a pump pulse (Pump) or a test magnetic field along the z direction $\lambda_{s,z} \sim 0.001$ –0.1 T (blue and green lines). $\omega_{\text{pump}} = 1.47$ eV. The pump pulse is centered at 0.5 ps. The longer time-scale dynamics (over 10 ps) for θ_K and S_z has similar relaxation time independent of the generation method of spin imbalance and specific probe energies.

slight variations between each other due to sample preparation conditions and specific measurement techniques. The spin lifetime increases from tens of picoseconds at room temperature to tens of nanoseconds at low temperature. Note that e-e scattering plays an essential role at low temperatures, i.e., by comparing with (black solid square) and without (black open square) in Fig. 3. The correct temperature dependence of $\tau_{s,z}$ can be reproduced only if e-e scattering is included.

We further examine the contributions of different scattering mechanisms to carrier and spin lifetime, respectively, as a function of temperature. Different from spin lifetime

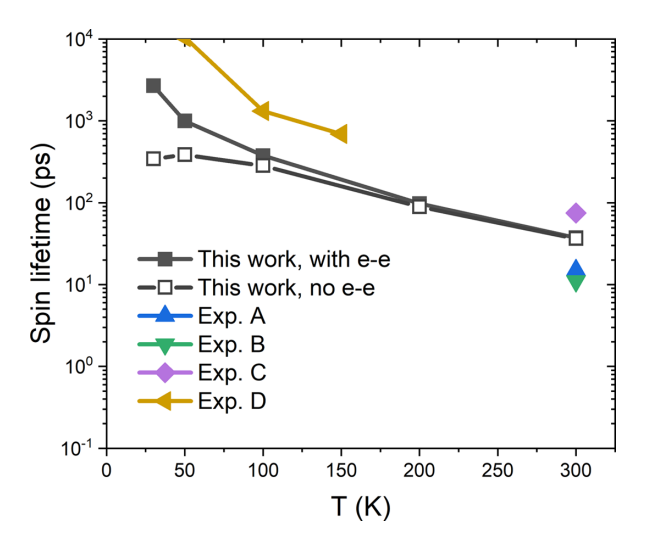


FIG. 3. Theoretical spin lifetime with (black solid square) and without (black open square) the electron-electron scattering compared with experimental data. A, B, C, and D are experimental data from Refs. [36], [81], [37], and [28], respectively.

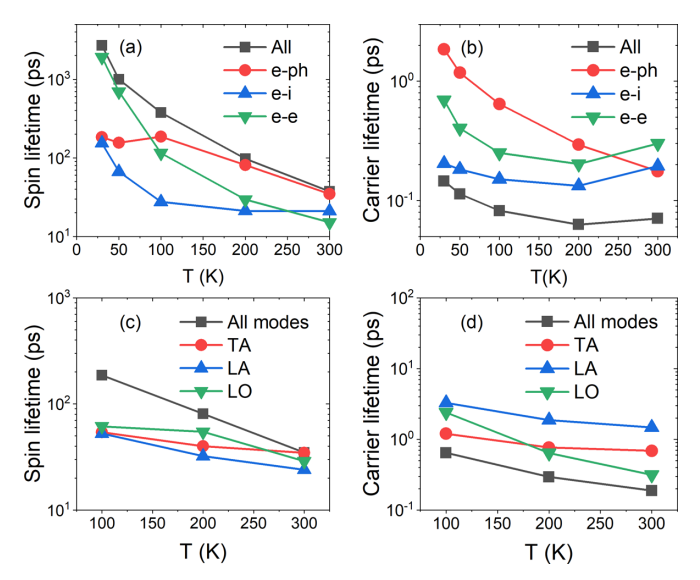


FIG. 4. Spin and carrier lifetimes of n-GaAs with $n_i=2\times 10^{16}~\rm cm^{-3}$ with different scattering mechanisms and different phonon modes. (a), (b) "All" represents all the e-ph, e-i, and e-e scattering mechanisms being considered. TA, LA, and LO represent transverse acoustic, longitudinal acoustic, and longitudinal optical modes, respectively. The carrier lifetimes $\overline{\tau}_p$ present are the inverse of averaged carrier scattering rates $\langle \tau_p^{-1} \rangle$. The method of carrier lifetime calculations is given in Appendix B. () means taking the average around the chemical potential μ . For a state-resolved quantity A_{kn} , its average is defined as $\langle A \rangle = \sum_{kn} A_{kn} [f^{\rm eq}]'(\epsilon_{kn}) / \sum_{kn} [f^{\rm eq}]'(\epsilon_{kn})$, where $[f^{\rm eq}]'$ is the derivative of the Fermi-Dirac function.

obtained from real-time DM dynamics including all scattering processes simultaneously, the carrier lifetime $(\overline{\tau}_p)$ is defined through the inverse of the averaged carrier scattering rate (τ_p^{-1}) : $\overline{\tau}_p = 1/\langle \tau_p^{-1} \rangle$. Various scattering processes (e-e, e-i, and e-ph) contribute to the total carrier scattering rates through $\tau_p^{-1} = (\tau_p^{e\text{-}e})^{-1} + (\tau_p^{e\text{-}i})^{-1} + (\tau_p^{e\text{-ph}})^{-1}$. $\langle \rangle$ means taking the average around the chemical potential μ . For a state-resolved quantity A_{kn} , its average is defined as $\langle A \rangle = \sum_{kn} A_{kn} [f^{\rm eq}]'(\epsilon_{kn}) / \sum_{kn} [f^{\rm eq}]'(\epsilon_{kn})$, where $[f^{\rm eq}]'$ is the derivative of the Fermi-Dirac function. For both carrier and spin lifetime, the lifetime due to the most dominant scattering channel is the closest to the one including all processes [black squares in both Figs. 4(a) and 4(b)]. For spin relaxation in Fig. 4(a), at low temperature below 50 K, e-e scattering is the most dominant process as discussed above. However, the e-ph process becomes more dominant above 100 K. On the other hand, for carrier relaxation in Fig. 4(b), the e-i process is dominant over a wide temperature range from low to right below room temperature. At room temperature, for both spin and carrier lifetimes, the e-ph scattering is the most important process (closest to the total lifetime with all scattering processes).

Our observations differ from those in Refs. [31,40], where the authors also found that e-e scattering dominates spin relaxation at lower temperatures, e.g., 77 K, but their results showed that at room temperature e-e scattering can be more important than other scatterings and enhances $\tau_{s,z}$ of n-GaAs by about 100% with moderate doping concentrations. The overestimate of the effects of e-e scattering at room

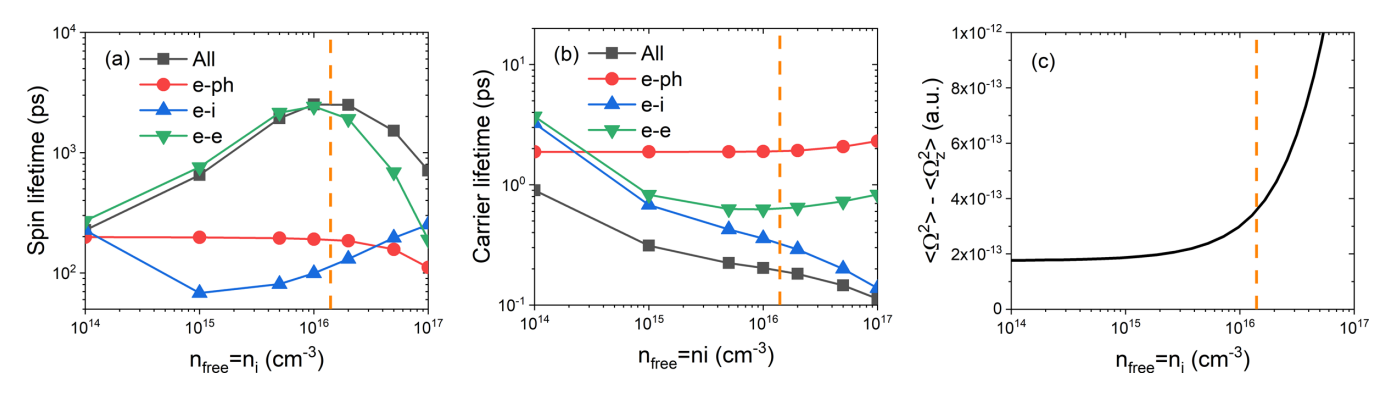


FIG. 5. (a) Spin and (b) carrier lifetimes of *n*-GaAs with different doping concentrations at 30 K with different scattering mechanisms. "All" represents all the *e*-ph, *e*-i, and *e*-*e* scattering mechanisms being considered. (c) $\langle \Omega^2 \rangle - \langle \Omega_i^2 \rangle$ as a function of carrier density, where Ω is the Larmor frequency due to the "internal" magnetic field computed from first principles, which describes the SOC term induced by inversion asymmetry.

temperature is most likely a limitation of the semiclassical method employed therein.

Similarly, we also find that different phonon modes can play different roles in carrier and spin relaxations as shown in Figs. 4(c) and 4(d). For example, at room temperature, the longitudinal optical (LO) mode is most important for carrier relaxation but seems less important than transverse acoustic (TA) modes for spin relaxation. The situation is the opposite at 100 K where TA (LO) is most important for carrier (spin) relaxation. Our finding that TA modes are slightly more important than LO modes in spin relaxation at room temperature is different from what has been believed in previous model studies [30,40], where they declared that the electron-LO-phonon scattering dominates spin relaxation at high temperatures especially at room temperature. This disparity is most likely due to differences in the e-ph matrix elements and electronic quantities, where we used fully first-principles approaches instead of parametrized models in previous work.

In addition, we find the total spin lifetime is the longest when considering all scattering processes in Fig. 4(a); in contrast, the carrier lifetime is the shortest including all scattering mechanisms in Fig. 4(b). This follows the inverse relation between spin and carrier lifetime in the empirical DP mechanism [2,14] for systems without inversion symmetry, as will be discussed in more detail in the next section.

3. Doping-level dependence of spin lifetime and its dominant relaxation mechanism

Figure 5 shows the carrier and spin lifetimes with different doping density n_i at 30 K with individual and total scattering pathways, respectively. Similar to temperature dependence and phonon contributions, it is also found that the roles of different scattering mechanisms differ considerably between spin and carrier relaxation processes. Specifically, for the carrier relaxation in Fig. 5(b), except when n_i is very low (e.g., at 10^{14} cm⁻³), the electron-impurity (*e*-i) scattering dominates, similar to the case of carrier lifetime over a large range of temperature at a moderate doping in Fig. 4(b). On the other hand, for the spin relaxation in Fig. 5(a), the *e-e* scattering dominates except at very high concentration (above

 10^{17} cm⁻³), while *e*-i scattering is only important in the very high doping region (close to or above 10^{17} cm⁻³).

Figure 5 shows the calculated τ_s has a maximum at $n_i =$ $(1-2) \times 10^{16}$ cm⁻³, and τ_s decreases quickly with n_i going away from its peak position. This is in good agreement with the experimental finding in Ref. [28], which also reported τ_s at $n_i = 10^{16} \text{ cm}^{-3}$ is longer than τ_s at other lower and higher n_i at a low temperature (a few kelvin). The n_i dependence of τ_s may be qualitatively interpreted from the commonly used empirical DP relation [2] for inversion-asymmetric systems, $\tau_{s,i} \sim \tau_{s,i}^{DP} = 1/[\overline{\tau}_p \cdot (\langle \mathbf{\Omega}^2 \rangle - \langle \Omega_i^2 \rangle)], \text{ where } \overline{\tau}_p \text{ is the carrier}$ lifetime, and Ω is the Larmor frequency due to the "internal" magnetic field, which describes the SOC term induced by inversion asymmetry. For spin-1/2 systems, the internal magnetic field at **k** (Ω_k) will induce an energy splitting Δ_k and polarize the spin along the direction of Ω_k . Previously, Ω_k was mostly obtained with a model Hamiltonian with Dresselhaus SOC field [82], which is rather qualitative. Instead, we obtained a k-dependent internal magnetic field Ω_k from firstprinciples calculations, by using $\Omega_{\mathbf{k},i} = 2\Delta_{\mathbf{k}} \cdot s_{\mathbf{k},i}^{\exp}/\hbar$, where $s_{\mathbf{k},i}^{\text{exp}}$ is the spin expectation value.

From Fig. 5, we find that with n_i from 10^{14}cm^{-3} to 5×10^{15} cm⁻³, carrier lifetime $\overline{\tau}_p$ decreases rapidly [black curve in Fig. 5(b)] and $\langle \Omega^2 \rangle - \langle \Omega_i^2 \rangle$ remains flat in Fig. 5(c), which may explain why spin lifetime (τ_s) increases in Fig. 5(a) based on the DP relation; however, when $n_i > 10^{16}$ cm⁻³, $\overline{\tau}_p$ decreases with a similar speed but $\langle \Omega^2 \rangle - \langle \Omega_i^2 \rangle$ experiences a sharp increase, which may explain why spin lifetime decreases in Fig. 5(b) and owns a maximum at 10^{16} cm⁻³.

Note that although the above empirical DP relation is intuitive to understand the cause of doping-level dependence of spin lifetime, it may break down when we evaluate individual scattering processes. For example, when n_i increases from 10^{14} to 10^{15} cm⁻³, both carrier lifetime $\overline{\tau}_p$ and spin lifetime $\tau_{s,z}$ due to e-i scattering decrease while the internal magnetic field remains unchanged. Moreover, the simple empirical relation cannot possibly explain our first-principles results that the e-e and e-i scatterings have largely different contributions in carrier and spin relaxation. First-principles calculations are critical to provide unbiased mechanistic insights to spin and carrier relaxation of general systems.

B. Applications to few-layer WSe₂

1. Spin-valley relaxation of resident holes of monolayer WSe2

For holes of monolayer WSe₂, spin-valley relaxation is mostly determined by intervalley spin-flip scattering processes between K and K' valleys because of the spin-valley locking. Previously, we reported spin-valley lifetimes of resident holes of monolayer TMDs at $T \ge 50$ K with e-ph scattering [27]. At very low temperatures, e.g., 10 K, intervalley e-ph scattering is, however, not activated as the corresponding phonon occupation is negligible; therefore, other scattering mechanisms are necessary to be included. Note that e-e scattering should not play an important role in spin relaxation of holes of TMDs. The reason is that the e-e scattering is a two-particle process where a transition is accompanied by another transition with energy and momentum being conserved. Considering the fact that only the highest occupied band is involved (see band structure in Fig. S5 [63]) in dynamics of TMD holes, for an e-e process, a $K \to K'$ ($K' \to K$) spin-flip transition must be accompanied by an opposite $K' \to K$ $(K \to K')$ spin-flip transition. Overall, e-e scattering processes have negligible contributions to spin relaxation of TMD semiconductors. As a result, we will include only e-ph and e-i scatterings for WSe2. We use the supercell method to compute e-i scattering matrix elements for neutral defects with self-consistent SOC and more details can be found in Appendix A.

Experimentally several types of impurities or defects exist in TMD samples. Here we pick four types of impurities with different symmetries and chemical bonds [see Fig. 6(a)]: Se vacancy (V_{Se}) , two neighboring Se vacancies (V_{2Se-N}) , W vacancy (V_W), and two Se vacancies with the same inplane position (V_{2Se-S}) . As most point defects are relatively deep with large ionization energies in semiconducting TMDs [85], we mostly consider neutral defects here. According to Refs. [86–88], the impurity concentration n_i ranges from 8×10^{10} to 10^{14} cm⁻² depending on samples. Considering that V_{Se} is often regarded as the most abundant impurity, we choose a reasonable impurity density n_i of V_{Se} , 7×10^{11} cm⁻², within the experimental range and for better comparison with experimental τ_s at $T \ge 20$ K shown in Fig. 6(b). n_i of V_{2Se-N} is chosen as 8×10^9 cm⁻², two orders of magnitude lower than V_{Se} because of its larger formation energy [88] and better comparison with experimental τ_s . n_i of V_W and V_{2Se-S} are chosen arbitrarily as we find they have rather weak effects on spin relaxation and are 7×10^{11} and $3.5 \times 10^{11} \text{cm}^{-2}$, respectively.

From Fig. 6, we first find that at T > 20 K, spin relaxation is almost driven by e-ph scattering and impurities can only affect spin relaxation at $T \le 20$ K. For the effects of different impurities on spin relaxation, we have $V_{2Se-N} \gg V_{Se} \gg V_{W} \sim V_{2Se-S}$. Such differences are directly related to the large differences among various impurities in electron-impurity matrix elements for the intervalley processes (scattering between K and K' valley), i.e., much larger matrix elements $|g_i|$ for intervalley scattering at V_{2Se-N} and V_{Se} compared to the ones at V_{W} and V_{2Se-S} as shown in SM Fig. S9 [63]. Moreover, the temperature dependence of τ_s with V_{2Se-N} is much weaker and in better agreement with experiments than that with V_{Se} . Therefore, the observed weak

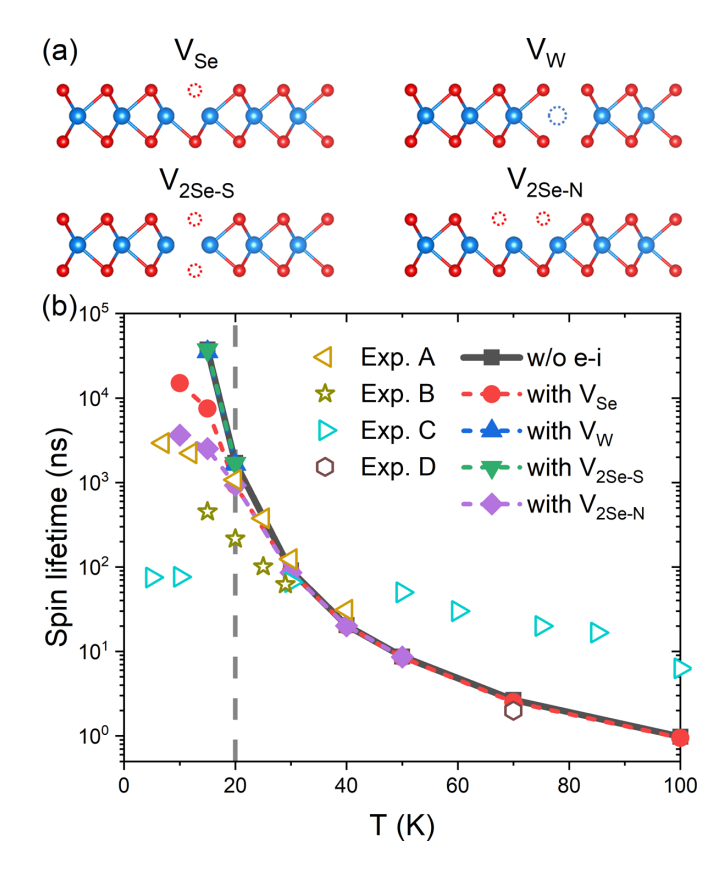


FIG. 6. (a) The schematics of four types of impurities in WSe₂. (b) Spin lifetimes of holes of monolayer WSe₂ with a relatively low hole density 10^{11} cm⁻² with impurities compared with experimental data. A, B, C, and D are experimental data from Refs. [42], [83], [46], and [84], respectively. The choices of impurity concentration n_i of different impurities are given in the main text.

temperature dependence in some experiments is probably related to the existence of larger size impurities with lower symmetries (e.g., V_{2Se-N}). Our observations suggest that the local symmetry and chemical bonds surrounding an impurity have a large impact on spin relaxation.

Additionally, we have simulated spin lifetimes of monolayer WSe₂ at 15 K with different hole densities and find a strong hole density dependence. The related results are shown in SM Fig. S12 [63].

2. Ultrafast dynamics of holes of bilayer WSe₂

Understanding detailed dynamical processes and related scattering mechanisms can help develop a strategy of controlling and manipulating spin-valley relaxation through tuning external fields, materials composition, and strain. In the following, we will first identify the scattering pathways of excited holes and spins in bilayer WSe₂ [AB stacking as shown in Fig. 7(a)]. Next, through real-time simulations, we determine dynamical quantities like spin lifetimes and valley polarization at different external fields and strain. Finally, we show the carrier occupation on each layer is fully spin polarized and can be switched by an external electric field.

According to previous studies [89,90] and our calculations, for valence bands of unstrained bilayer WSe₂, the Γ valley is slightly higher than the K/K' valley, which is usually

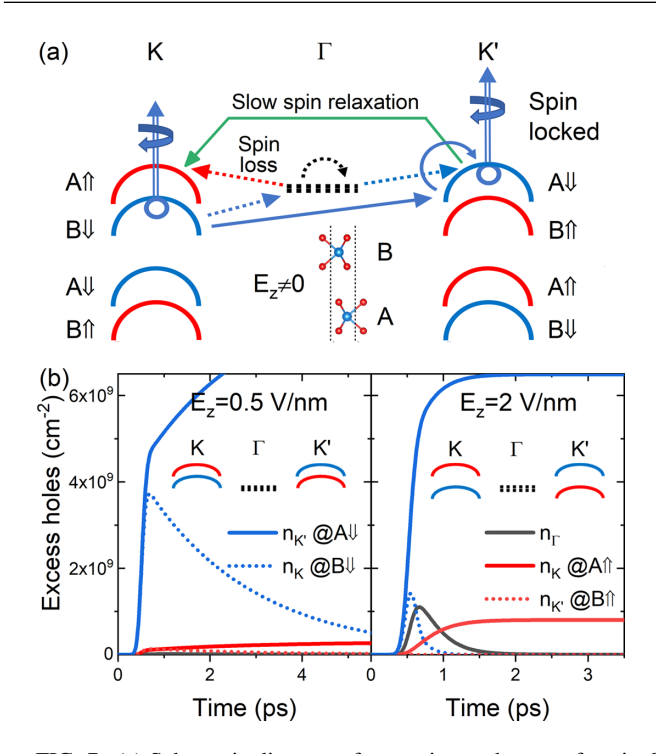


FIG. 7. (a) Schematic diagram of scattering pathways of excited holes in 1% compressed bilayer WSe2 with a low equilibrium hole density and $1.4 \times 10^{12}~\text{cm}^{-2}~\text{V}_{\text{Se}}$ (double the monolayer value in Fig. 6) under finite E_z during and after a circularly polarized pump, which initially excite holes (labeled as half circles) at both K and K' valleys and two top valence bands ("A \downarrow " at K' and "B \downarrow " at K). The lower-energy excited holes will decay to the band edge (most to " $A \downarrow$ " at K' and fewer to " $A \uparrow$ " at K) through different scattering pathways. A state being labeled by "A" ("B") means the wavefunction of this state is mostly localized in layer A (B) of the bilayer. \uparrow and ↓ represent spin up and spin down, respectively. The color of the electronic state represents spin polarization: red and blue mean spin up and spin down, respectively. (b) Time evolutions of valley- and band-resolved (excited or excess) hole densities at 50 K under two E_z with a circularly polarized pump. The pump energy is selected to excite electrons at two top valence bands. The pump center is at 0.5 ps. n_V represents excess hole density at valley V. The insets of (b) are the schematics of energies of two top valence bands at K, K'and Γ valleys under two E_z (see calculated band structures in SM Fig. S7).

undesirable. The K/K' valley can be pushed higher than the Γ valley by applying slight in-plane compressive strain (corresponding band structures can be found in SM Fig. S6 [63]). Moreover, under zero E_z , the bilayer WSe₂ has inversion symmetry, leading to carriers being equally populated at K and K' valleys and at two layers, with spin-up and -down degeneracy. A finite E_z can break inversion symmetry (thus breaking Kramers degeneracy) and induce nonzero layer polarization or layer population difference. For example, two top valence bands from layer A with ↑ (up spin) and layer B with \downarrow (down spin) are degenerate at K without electric field but split under electric field. Thus each band is associated with a particular spin channel, valley, and layer, i.e., a spin-valleylayer locking effect. Also by tuning the sign and magnitude of E_z , we are able to control various physical quantities like layer pseudospin, band splitting energy, etc. Therefore, to ensure spin-valley-layer locking effects being observed, we will study slightly compressed inversion-symmetric bilayer WSe₂ under finite E_z .

Figure 7(a) shows the scattering pathway schematics for hole bands (half circles) during the first few picoseconds of slightly compressed (1%) bilayer WSe₂ excited by a circularly polarized pump pulse under finite E_7 at 50 K, before exciton recombination processes happen typically at the tens of picoseconds time scale at this temperature [91,92]. Similar to the GaAs case (see Sec. IV A 1), the hole spins will undergo the following processes: optical generation, decay to band edges, and at the end slow relaxation. Initially, holes with the same spin polarization are excited at both K and K' valleys and two layers equally [e.g., down-spin holes generated at the K valley and layer B and K' valley and layer A as shown in Fig. 7(a)]. During and after the excitations, lower-energy holes at the K(K') valley will decay to the band edge through two possible scattering pathways: (i) a direct pathway through interlayer spin-conserving scattering (solid blue line) or (ii) an indirect pathway through Γ -valley-related scattering (dashed lines for both spin-conserving and -flip processes). After all holes decay to the band edge, most of their carried spins are "locked" at a certain layer and valley (e.g., "A \downarrow " at K'in Fig. 7) due to weak intervalley spin-flip scattering [green arrow in Fig. 7(a)], which is the so-called spin-valley-layer

In Fig. 7(b), we show time evolutions of valley- and bandresolved (excited or excess) hole densities under two E_z . It can be seen that under a low E_z [0.5 V/nm, Fig. 7(b), left panel], the main scattering pathway is the direct one mentioned above, i.e., the spin-down holes scattered from B \downarrow at K in the dashed blue line with decreasing population to A \downarrow at K' in the solid blue line with increasing population. Under a higher E_z [2 V/nm, right panel of Fig. 7(b)], although the direct scattering pathway still exists, the indirect one through the Γ valley also becomes important because the band energy at Γ is pushed higher than the second valence band at Kand K' under this electric field [see inset of Fig. 7(b), right panel]. Here occupation at B \downarrow at K in the dashed blue line rapidly decreased while occupation at Γ with both up and down spins in solid black temporarily increased through indirect scattering, and most importantly the A \uparrow at K in solid red also increased due to the scattering through the Γ valley. Increased population at A \uparrow at K represents weakening of the spin-valley-locking effect. Therefore, the indirect scattering pathway will lead to the reduction of spin density and valley polarization.

We then show two key dynamical quantities: spin lifetime τ_s in Fig. 8(a) and maximum valley polarization of bilayer WSe₂ in Fig. 8(b) as a function of E_z with different percentages of strain. Valley polarization is defined as $P_V = |n_K - n_{K'}|/n_{tot}$, where $n_{K(K')}$ is excess hole density at the K(K') valley and n_{tot} is total excess hole density. A high maximum of P_V is necessary to ensure a high P_V for extended time. This is because when P_V reaches its maximum, since most carriers and/or spins have already decayed to the band edge at the same time, P_V will decay very slowly through intervalley spin-flip scattering. Obviously, an unstrained system is not suitable to utilize spin-valley-layer locking considering its short spin lifetimes and low maximum P_V under a relatively

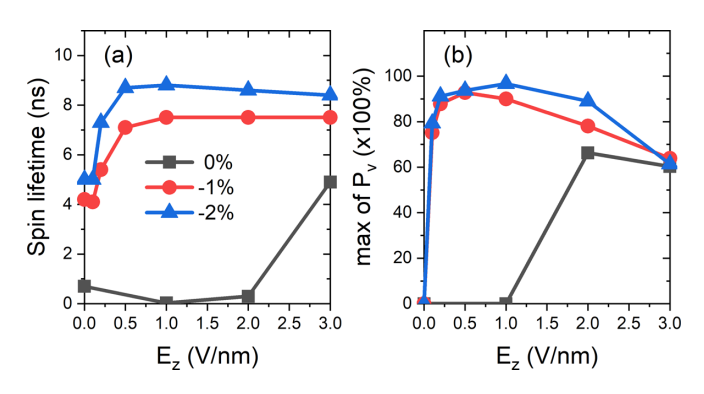


FIG. 8. Spin lifetime and maximum valley polarization $P_V = |n_K - n_{K'}|/n_{tot}$ of bilayer WSe₂ at 50 K, where $n_{K(K')}$ is excess hole density at the K (K') valley and n_{tot} is total excess hole density. Negative strain means compressive strain. P_V will be 90% of its maximum shortly after the pump and reach the maximum at a time from 1 to 20 ps depending on E_z and the strain. After reaching its maximum, since most carriers and/or spins have already decayed to the band edge, P_V can relax only very slowly through intervalley spin-flip scattering. This implies that having a high maximum of P_V is important to ensure a high P_V during a long time.

low electric field. As we discussed above, a slight strain is helpful to ensure K or K' valleys are sufficiently higher than the Γ valley. Moreover, from Fig. 8, an optimized range of E_z is from \sim 0.2 to \sim 2 V/nm, where the system shows long τ_s and high maximum P_V , consistent with the fact mentioned above: the indirect scattering pathway, which becomes important under high E_z , will cause loss of spin and valley polarization.

Finally, in a bilayer, the percentage of carriers and/or spins localized in the top or bottom layer at equilibrium can be controlled by a static E_z . For device applications, it may be desirable to dynamically and spatially tune the locations of holes and/or spins by controlling E_z . For this purpose, a knowledge of the speed of carriers and spins transferring between two layers can be useful.

To extract the time scale of such a transfer, we first generate holes and/or spins by applying a circularly polarized pump pulse centered at -9.5 ps and let the system evolves until t=0 under $E_z=0.5$ V/nm to ensure almost all holes and/or spins are localized in the bottom layer, then by switching E_z suddenly to -0.5 V/nm at t=0, holes and/or spins will start to transfer to the top layer.

In Fig. 9, we show the time evolution of top-layer hole occupation f_h^{top} and spin s_z^{top} (see their definitions in Appendix D) normalized by corresponding total quantities of 2% compressed bilayer after the sign of E_z is switched. From Fig. 9, at 50 K, 90% switching of f_h^{top} and s_z^{top} takes \sim 6 ps. This time constant is much shorter than τ_s , which means such tuning is fast enough to use an electric field as a "switch" in spintronic devices.

V. CONCLUSIONS

In this article, we present a first-principles real-time density-matrix approach to simulate ultrafast spin-orbit-mediated spin dynamics in solids with arbitrary crystal symmetry. The complete *ab initio* descriptions of pump, probe, and three scattering processes—the electron-phonon,

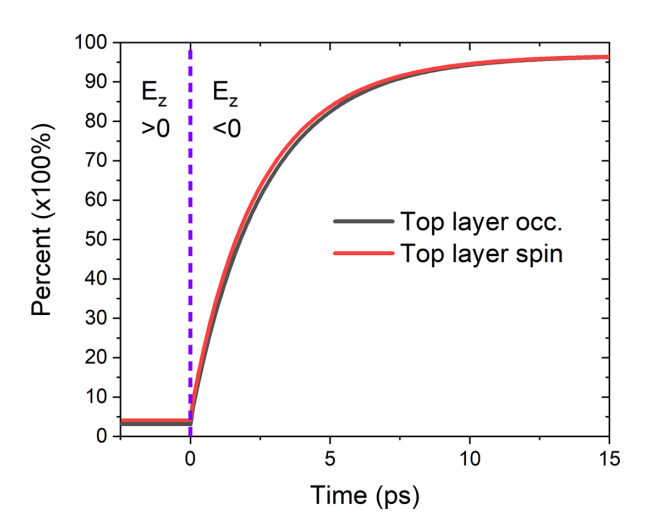


FIG. 9. Time evolution of top layer hole occupation f_h^{top} and spin s_z^{top} (see their definitions in Appendix D) normalized by corresponding total quantities of compressed bilayer WSe₂ at 50 K after the sign of E_z is switched at t=0. At t=-10 ps, a pump pulse centered at t=-9.5 ps with $\tau_{\text{pump}}=100$ fs is started to be applied and real-time density matrix dynamics is run under $E_z=0.5$ V/nm until t=0 to allow holes and spins to decay to the band edge where states are localized in bottom layer. When the sign of E_z is suddenly switched, holes and spins are still localized in the same bottom layer but the new eigenstates around the band edge are localized in the top layer; thus holes and spins will transfer from the bottom to the top layer.

electron-impurity, and electron-electron scattering in the density-matrix master equation—allow us to directly simulate the nonequilibrium ultrafast pump-probe measurements and make our method applicable to any temperatures and doping levels. This method has been applied to simulate spin relaxation of *n*-GaAs. We confirm that the relaxation time of Kerr rotation and that of spin observables are almost identical and find that the relaxation time of spin polarization is relatively robust, i.e., insensitive to how spin imbalance is initialized. Furthermore, we have studied the temperature and dopinglevel dependencies of spin lifetime and examined the roles of various scattering mechanisms. Overall our theoretical results are in good agreement with experiments. Importantly, our first-principles simulations provide rich mechanistic insights of spin relaxation of n-GaAs: we point out that although at low temperatures and moderate doping concentrations e-i scattering dominates carrier relaxation, e-e scattering is the most dominant process in spin relaxation. The relative contributions of phonon modes also vary considerably between spin and carrier relaxation. We have further examined ultrafast dynamics in few-layer WSe₂ with realistic impurities. We find that spin relaxation can highly depend on local symmetry and chemical bonds surrounding impurities. For the bilayer, we identify the scattering pathways of holes in ultrafast dynamics and determine relevant dynamical properties, including τ_s , maximum valley polarization, and layer population and spin switch time, which are essential to utilize its unique spin-valley-layer locking effects. Our method opens up the pathway to predict spin relaxation and decoherence for general materials and provides unbiased insights and guidelines to experimental materials design, which have the potential to revolutionize the field of spintronics and quantum information technologies.

ACKNOWLEDGMENTS

We thank Hiroyuki Takenaka for helpful discussions. This work is supported by the National Science Foundation under Grant No. DMR-1956015 and the Air Force Office of Scientific Research under AFOSR Award No. FA9550-YR-1-XYZQ. A.H. acknowledges support from the American Association of University Women (AAUW) fellowship program. This research used resources of the Center for Functional Nanomaterials, which is a U.S. DOE Office of Science Facility, and the Scientific Data and Computing center, a component of the Computational Science Initiative, at Brookhaven National Laboratory under Contract No. DE-SC0012704, the lux supercomputer at the University of California, Santa Cruz, funded by NSF MRI Grant No. AST 1828315, the National Energy Research Scientific Computing Center (NERSC), a U.S. Department of Energy Office of Science User Facility operated under Contract No. DE-AC02-05CH11231, the Extreme Science and Engineering Discovery Environment (XSEDE), which is supported by National Science Foundation Grant No. ACI-1548562 [93], and resources at the Center for Computational Innovations at Rensselaer Polytechnic Institute.

APPENDIX A: INTERACTION HAMILTONIAN TERMS AND MATRIX ELEMENTS

Three interaction Hamiltonian terms in Eq. (3) read

$$H_{e-ph} = \sum_{12q\lambda} c_1^{\dagger} c_2 (g_{12}^{q\lambda} - b_{q\lambda} + g_{12}^{q\lambda} + b_{q\lambda}^{\dagger}), \tag{A1}$$

$$H_{e-i} = n_i V_{\text{cell}} \sum_{12} c_1^{\dagger} c_2 g_{12}^i,$$
 (A2)

$$H_{e-e} = \sum_{1234} c_1^{\dagger} c_2^{\dagger} c_3 c_4 g_{1234}^{e-e}. \tag{A3}$$

The *e*-ph matrix $g^{q\lambda\pm}$ is computed with self-consistent spin-orbit coupling and Wannier interpolation by the supercell method.

Here we assume impurity density is sufficiently low and the average distance between neighboring impurities is sufficiently long so that the interactions between impurities are negligible. The e-i matrix g^i is

$$g_{13}^i = \langle 1|\Delta V^i|3\rangle,\tag{A4}$$

$$\Delta V^i = V^i - V^0, \tag{A5}$$

where V^i is the potential of the impurity system and V^0 is the potential of the pristine system. In this work, g^i for neutral and ionized impurities are computed differently as follows.

For neutral impurities, V^i is computed using a large supercell including an impurity with self-consistent SOC at DFT. This is important for including the detailed potential profile and chemical bonding environment for different impurities. To speed up the supercell convergence, we used the potential alignment method developed in Ref. [94]. We checked the supercell size convergence of g^i for neutral V_{Se} in monolayer

WSe₂ and found that the corresponding spin lifetime with 6×6 and 8×8 supercells differs by only a few percent. Thus the 6×6 supercell is enough for g^i of neutral impurities in monolayer WSe₂.

For ionized impurities, we use approximate impurity potentials as detailed below. In general, ΔV^i may be separated into two terms $\Delta V^i = \Delta V^i_{\rm ns} + \Delta V^i_{\rm soc}$, where $\Delta V^i_{\rm ns}$ is the spin-independent part and $\Delta V^i_{\rm soc} = [\hbar/(4m^2c^2)]\nabla(\Delta V^i_{\rm ns})\times {\bf p}\cdot \sigma$ is the SOC correction. For ionized impurities, we approximate $\Delta V^i_{\rm ns}$ as the potential of point charge which is simply the product of the impurity charge Z and the screened Coulomb potential [54], i.e., $\Delta V^i_{\rm ns} = ZV^{\rm scr}$. Such an approximation describes the long-range part of the spin-independent differential impurity potential $\Delta V^i_{\rm ns}$ accurately, which is often the most important contribution from ionized impurities. Considering that $\Delta V^i_{\rm soc}$ is commonly neglected in previous theoretical studies on spin relaxation [30,95] whenever the screened Coulomb potential $V^{\rm scr}$ is used, we will not include $\Delta V^i_{\rm soc}$ for ionized impurities either. Note that such potential for ionized impurities still relaxes spin through spin mixing and spin precession.

The e-e matrix g^{e-e} is

$$g_{1234}^{e-e} = \langle 1(r)|\langle 2(r')|V(r-r')|3(r)\rangle|4(r')\rangle,$$
 (A6)

where V(r-r') is the screened electron-electron interaction. The SOC corrections on V(r-r') [96,97] will not be included, similar to the ionized impurity case. Thus, V(r-r') is simply the screened Coulomb potential V^{scr} . Therefore, in both calculations of g^i and g^{e-e} , the computation of the screened Coulomb potential V^{scr} is of key importance.

Currently, we use the static RPA dielectric function for the screening and neglect local-field effects. We then show that the e-e self-energy (Im Σ) obtained with such a dielectric function well reproduces the one obtained with dynamically screened Coulomb interaction with full RPA dielectric matrix in the relevant energy range as shown in Fig. 10. The dielectric function has the form

$$\epsilon(\mathbf{q}) = \epsilon_s \epsilon^{\text{intra}}(\mathbf{q}),$$
 (A7)

where ϵ_s is the static background dielectric constant and can be calculated by density functional perturbation theory (DFPT) [98]. $\epsilon^{\text{intra}}(\mathbf{q})$ is the intraband contribution which involves only states with free carriers and is critical for doped semiconductors. It is computed using RPA,

$$\epsilon^{\text{intra}}(\mathbf{q}) = 1 - V^{\text{bare}}(\mathbf{q}) \sum_{\mathbf{k}mn} \times \left(\frac{f_{\mathbf{k}-\mathbf{q},m} - f_{\mathbf{k}n}}{\epsilon_{\mathbf{k}-\mathbf{q},m} - \epsilon_{\mathbf{k},n}} \times |\langle u_{\mathbf{k}-\mathbf{q},m} | u_{\mathbf{k}n} \rangle|^2 \right), \quad (A8)$$

where the sum runs over only states having free carriers, e.g., for a n-doped semiconductor, m and n are conduction-band indices. In the above formula, f is time-dependent nonequilibrium occupation instead of the equilibrium one, $f^{\rm eq}$. Therefore, if the pump is activated or the optical field ${\bf A}_0(t)$ of the pump pulse is not negligible, $\epsilon^{\rm intra}({\bf q})$ will be updated in every time step, as f will differ from $f^{\rm eq}$ and the magnitude of difference depends on the excitation density. $V^{\rm bare}({\bf q}) = e^2/(V_{\rm cell} \varepsilon_0 |q|^2)$ is the bare Coulomb potential with $V_{\rm cell}$ the unit cell volume and ε_0 vacuum permittivity. $u_{{\bf k}n}$ is the periodic part of the Bloch wave function.

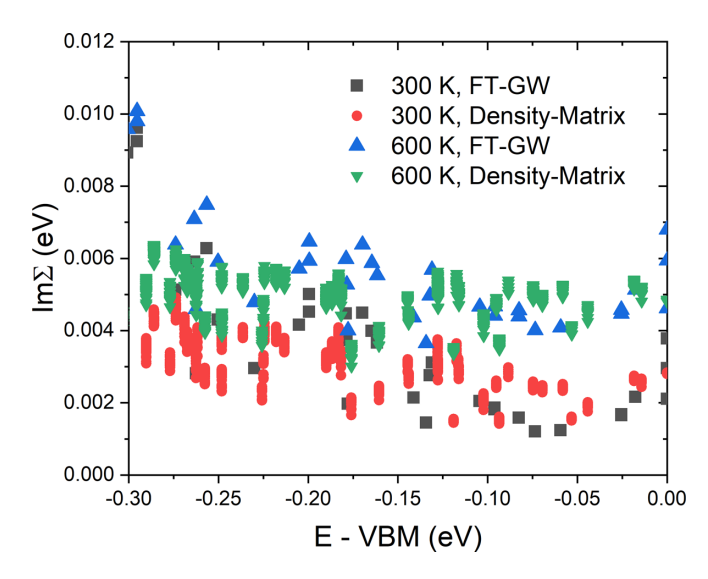


FIG. 10. Im Σ due to *e-e* scattering of valence electrons of *p*-type silicon computed by Eq. (B5) (density-matrix) compared with those calculated by the finite-temperature GW method (FT-GW), where G is Green's function and W is the screened Coulomb potential [100]. μ is set to 0.05 eV lower than the valence-band maximum (VBM). For simplicity, SOC is not considered in this test.

We then have the matrix elements in reciprocal space,

$$g_{13}^i = ZV^{\text{scr}}(\mathbf{q}_{13})\langle u_1|u_3\rangle, \tag{A9}$$

$$g_{1234}^{e-e} = V^{\text{scr}}(\mathbf{q}_{13})\delta_{\mathbf{k}_1 + \mathbf{k}_2, \mathbf{k}_3 + \mathbf{k}_4} \langle u_1 | u_3 \rangle \langle u_2 | u_4 \rangle, \tag{A10}$$

$$V^{\text{scr}}(\mathbf{q}_{13}) = V^{\text{bare}}(\mathbf{q}_{13})/\epsilon(\mathbf{q}_{13}),$$
 (A11)

where $V^{\text{scr}}(\mathbf{q})$ is the screened Coulomb potential and $\mathbf{q}_{13} = \mathbf{k}_1 - \mathbf{k}_3$. $\delta_{\mathbf{k}_1 + \mathbf{k}_2, \mathbf{k}_3 + \mathbf{k}_4}$ is the Kronecker delta function and means $\mathbf{k}_1 + \mathbf{k}_2 = \mathbf{k}_3 + \mathbf{k}_4$. $\langle u_1 | u_3 \rangle$ is the overlap matrix element between two periodic parts of the Bloch wave functions.

APPENDIX B: CARRIER SCATTERING RATE AND Im Σ FROM THE DENSITY-MATRIX APPROACH

At the semiclassical limit, density matrix ρ is replaced by (nonequilibrium) occupation f; then the scattering term originally with a full quantum description in Eq. (9) required by DM dynamics becomes

$$\left. \frac{df_1}{dt} \right|_c = \sum_{2 \neq 1} \left[(1 - f_1) P_{11,22}^c f_2 - (1 - f_2) P_{22,11}^c f_1 \right], \quad (B1)$$

using the facts that $P_{11,22}$ is real and the "2 = 1" term is zero. "c" represent a scattering channel. Note that the weights of k points must be considered when doing a sum over k points.

Suppose f is perturbed from its equilibrium value by δf , i.e., $f = f^{\text{eq}} + \delta f$; then we insert f after perturbation into Eq. (B1) and linearize it,

$$\left. \frac{df_1}{dt} \right|_c = -\sum_{2 \neq 1} \left[P_{11,22}^c f_2^{\text{eq}} + (1 - f_2^{\text{eq}}) P_{22,11}^c \right] \delta f_1, \quad (B2)$$

using the fact that $\delta P_{11,22}$ is always zero, even for the *e-e* scattering.

Defining the carrier relaxation time of state "1," $\tau_{p,1}^c$, by $\frac{df_1}{dt}|_c = -\frac{\delta f_1}{\tau^c}$, we have

$$\frac{1}{\tau_{p,1}^c} = \sum_{2 \neq 1} \left[P_{11,22}^c f_2^{\text{eq}} + (1 - f_2^{\text{eq}}) P_{22,11}^c \right].$$
 (B3)

The linewidth or the imaginary part of the self-energy for the scattering channel c is related to the carrier relaxation time by $\operatorname{Im}\Sigma_1^c = \hbar/(2\tau_{p,1}^c)$.

Using Eq. (B3), we have calculated the *e*-ph scattering rates and they are in good agreement with previous theoretical results [99]. For *e*-ph scattering, Eq. (B3) will reproduce the imaginary part of the well-known Fan-Migdal self-energy [53].

For e-i scattering, we have

$$\frac{1}{\tau_{p,1}^{e-\mathrm{i}}} = \frac{2\pi}{\hbar} n_i V_{\text{cell}} \sum_{j} \left| g_{12}^i \right|^2 \delta_{\sigma}^G(\epsilon_1 - \epsilon_2). \tag{B4}$$

The above equation [Eq. (B4)] is consistent with Ref. [54].

For *e-e* scattering, neglecting the exchange contribution, which is a commonly used approximation [50,100],

$$\frac{1}{\tau_{p,1}^{e-e}} = \frac{2\pi}{\hbar} \sum_{2 \neq 1,34} |A_{1324}|^2 \begin{bmatrix} f_2^{eq} f_4^{eq} (1 - f_3^{eq}) + \\ (1 - f_2^{eq}) f_3^{eq} (1 - f_4^{eq}) \end{bmatrix}. \quad (B5)$$

To verify our implementation of the e-e scattering term, we calculate Im Σ due to e-e scattering of valence electrons of p-type silicon based on the above equation and compare it with those calculated by the finite-temperature GW method from first principles [100], as implemented in JDFTX [60]. The JDFTX implementation, in turn, has been benchmarked to reproduce the expected dependence with temperature and carrier energy, Im $\Sigma^{e-e} \propto (\varepsilon - \varepsilon_F)^2 + (\pi k_B T)^2$, as expected for metals [76].

From Fig. 10, we can see the results by two methods agree well for the energy range close to the Fermi level which is relevant to e-e scatterings due to energy conservation. This verifies our implementation of the e-e scattering part.

APPENDIX C: THE EFFECTS OF ω_{pump} AND PUMP FLUENCE ON SPIN RELAXATION OF GaAs AT 300 K

In Fig. 11, we study the S_z relaxation dependence on pump-pulse energy changes with several k_BT . We can see that variation of ω_{pump} has very weak effects on the spin dynamics of n-GaAs at 300 K.

In Fig. 12(a), we study the effects of the pump fluence I_{pump} on spin relaxation. First, we can see that in the low-pump-fluence region or when $I_{pump} < 1 \ \mu J/cm^{-2}$, the excitation density increases linearly with I_{pump} , but when $I_{pump} > 1 \ \mu J/cm^{-2}$, the excitation density increases more slowly. This is because in high-fluence cases, during the excitation by a pump pulse, a significant number of conduction states have been already filled, which reduces the probability of the transitions from valence bands to conduction bands. From Fig. 12(b), we find that the spin lifetime of n-GaAs decreases with the excitation density. This dependence may be explained based on the empirical DP relation [2] $\tau_{s,i} \sim \tau_{s,i}^{DP} = 1/[\overline{\tau}_p \cdot (\langle \Omega^2 \rangle - \langle \Omega_i^2 \rangle)]$ as we discussed in Sec. IV A 2. At 300 K, generally $\langle \Omega^2 \rangle - \langle \Omega_i^2 \rangle$ will increase with increasing

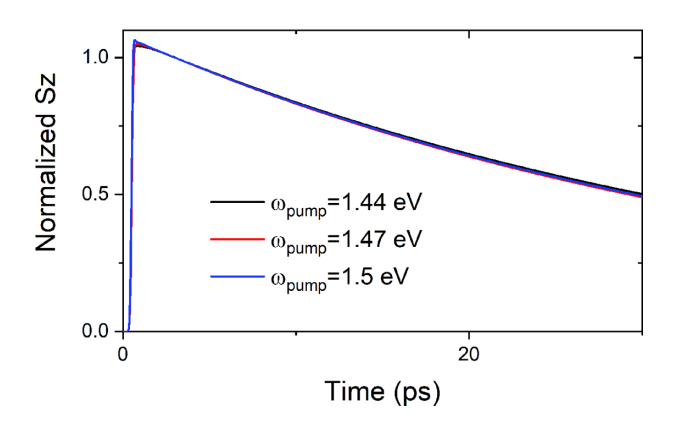


FIG. 11. $S_z(t)$ of *n*-GaAs with $n_i = 2 \times 10^{16}$ cm⁻³ at 300 K with different pump-pulse energies (ω_{pump}) varying with several k_BT .

free carrier density (through an increase of excitation density here), similar to what we find at 30 K shown in Fig. 5(c). On the other hand, $\overline{\tau}_p$ due to the electron-phonon scattering, which dominates carrier relaxation at 300 K, is less sensitive to the variation of excitation density. Therefore, it is the increase of $\langle \Omega^2 \rangle - \langle \Omega_i^2 \rangle$ causing the decrease of spin lifetime when increasing excitation density.

APPENDIX D: LAYER-RESOLVED QUANTITIES OF BILAYER WSe₂

For a bilayer with one layer above z=0 and another below, the operator \hat{l}^{top} projecting any local quantity $A(\mathbf{r})$ to the top layer can be defined through the relation

$$\hat{l}^{\text{top}}A(\mathbf{r}) = H(z)A(\mathbf{r}),\tag{D1}$$

where z is the third component of \mathbf{r} and H(z) is Heaviside step function:

$$H(z) = \begin{cases} 1, & z > 0 \\ 0, & z \le 0. \end{cases}$$
 (D2)

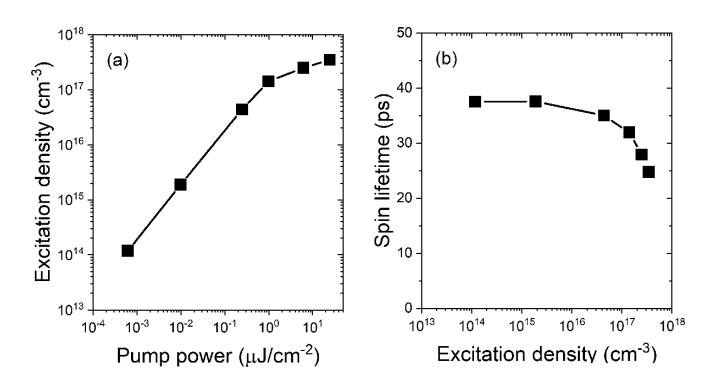


FIG. 12. (a) The excitation density as a function of the pump fluence (left panel) and (b) the spin lifetime as a function of the excitation density generated by a circularly polarized pump pulse for n-GaAs with $n_i = 10^{14}$ cm⁻³ at 300 K. $\omega_{\text{pump}} = 1.47$ eV.

Therefore, top layer hole occupation f_h^{top} is

$$f_h^{\text{top}} = \text{Tr}(\hat{l}^{\text{top}}(1-f)) \tag{D3}$$

$$= \sum_{k_n} l_{k,nn}^{\text{top}} (1 - f_{kn}), \tag{D4}$$

where f is occupation and $l_{k,mn}^{\text{top}} = \langle km | \hat{l}^{\text{top}} | kn \rangle = \langle km | H(z) | kn \rangle$, Tr means taking trace, k is a k-point index, and n and m are band indices.

Moreover, the top layer spin s_z^{top} can be defined using the operator $\hat{l}^{\text{top}}\hat{s}_z$,

$$s_z^{\text{top}} = \text{Tr}(\hat{l}^{\text{top}}\hat{s}_z\hat{\rho}) \tag{D5}$$

$$= \sum_{k,lmn} l_{k,lm}^{\text{top}} s_{z,k,mn} \rho_{k,nl}. \tag{D6}$$

Note that the commutator $[l^{top}, s_z]$ is found numerically close to zero for bilayer WSe₂. This indicates that we can safely define s_z^{top} as an observable using the above equations.

- [14] M. I. Dyakonov and V. I. Perel, Sov. Phys. Solid State **13**, 3023 (1972).
- [15] A. W. Cummings, J. H. Garcia, J. Fabian, and S. Roche, Phys. Rev. Lett. 119, 206601 (2017).
- [16] D. Afanasiev, A. Gatilova, D. J. Groenendijk, B. A. Ivanov, M. Gibert, S. Gariglio, J. Mentink, J. Li, N. Dasari, M. Eckstein, T. Rasing, A. D. Caviglia, and A. V. Kimel, Phys. Rev. X 9, 021020 (2019).

^[1] D. D. Awschalom, R. Hanson, J. Wrachtrup, and B. B. Zhou, Nat. Photonics 12, 516 (2018).

^[2] I. Žutić, J. Fabian, and S. D. Sarma, Rev. Mod. Phys. 76, 323 (2004).

^[3] F. Meier and B. P. Zakharchenya, *Optical Orientation* (Elsevier, Amsterdam, 2012).

^[4] M. P. M. Dean, Y. Cao, X. Liu, S. Wall, D. Zhu, R. Mankowsky, V. Thampy, X. M. Chen, J. G. Vale, D. Casa et al., Nat. Mater. 15, 601 (2016).

^[5] A. Avsar, H. Ochoa, F. Guinea, B. Özyilmaz, B. J. van Wees, and I. J. Vera-Marun, Rev. Mod. Phys. 92, 021003 (2020).

^[6] J. J. Pla, K. Y. Tan, J. P. Dehollain, W. H. Lim, J. J. L. Morton, D. N. Jamieson, A. S. Dzurak, and A. Morello, Nature (London) 489, 541 (2012).

^[7] J. Schliemann, Rev. Mod. Phys. 89, 011001 (2017).

^[8] C. E. Dreyer, A. Alkauskas, J. L. Lyons, A. Janotti, and C. G. Van de Walle, Annu. Rev. Mater. Res. 48, 1 (2018).

^[9] F. Wu, A. Galatas, R. Sundararaman, D. Rocca, and Y. Ping, Phys. Rev. Mater. 1, 071001(R) (2017).

^[10] T. J. Smart, F. Wu, M. Govoni, and Y. Ping, Phys. Rev. Mater. 2, 124002 (2018).

^[11] F. Wu, T. J. Smart, J. Xu, and Y. Ping, Phys. Rev. B **100**, 081407(R) (2019).

^[12] F. Wu, D. Rocca, and Y. Ping, J. Mater. Chem. C 7, 12891 (2019).

^[13] T. J. Smart, K. Li, J. Xu, and Y. Ping, Npj Comput. Mater. 7, 59 (2021).

- [17] M. W. Wu, J. H. Jiang, and M. Q. Weng, Phys. Rep. 493, 61 (2010).
- [18] R. Rosati, R. C. Iotti, F. Dolcini, and F. Rossi, Phys, Rev. B 90, 125140 (2014).
- [19] A. Habib, J. Xu, Y. Ping, and R. Sundararaman, arXiv:2012.11550.
- [20] O. D. Restrepo and W. Windl, Phys. Rev. Lett. 109, 166604 (2012).
- [21] J. Park, J. J. Zhou, and M. Bernardi, Phys, Rev. B 101, 045202 (2020).
- [22] D. V. Fedorov, M. Gradhand, S. Ostanin, I. V. Maznichenko, A. Ernst, J. Fabian, and I. Mertig, Phys. Rev. Lett. 110, 156602 (2013).
- [23] M. A. L. Marques, N. T. Maitra, F. M. S. Nogueira, E. K. U. Gross, and A. Rubio, *Fundamentals of Time-Dependent Den*sity Functional Theory (Springer Science & Business Media, 2012), Vol. 837.
- [24] Z. Chen and L. Wang, Sci. Adv. 5, eaau8000 (2019).
- [25] S. R. Acharya, V. Turkowski, G. P. Zhang, and T. S. Rahman, Phys. Rev. Lett. 125, 017202 (2020).
- [26] K. Krieger, J. K. Dewhurst, P. Elliott, S. Sharma, and E. K. U. Gross, J. Chem. Theory Comput. 11, 4870 (2015).
- [27] J. Xu, A. Habib, S. Kumar, F. Wu, R. Sundararaman, and Y. Ping, Nat. Commun. 11, 2780 (2020).
- [28] J. M. Kikkawa and D. D. Awschalom, Phys. Rev. Lett. 80, 4313 (1998).
- [29] D. J. Hilton and C. L. Tang, Phys. Rev. Lett. 89, 146601 (2002).
- [30] J. H. Jiang and M. W. Wu, Phys. Rev. B 79, 125206 (2009).
- [31] A. Kamra and B. Ghosh, J. Appl. Phys 109, 024501 (2011).
- [32] F. Dettwiler, J. Fu, S. Mack, P. J. Weigele, J. C. Egues, D. D. Awschalom, and D. M. Zumbühl, Phys. Rev. X 7, 031010 (2017).
- [33] D. Huber, M. Reindl, S. F. Covre Da Silva, C. Schimpf, J. Martín-Sánchez, H. Huang, G. Piredda, J. Edlinger, A. Rastelli, and R. Trotta, Phys. Rev. Lett. 121, 033902 (2018).
- [34] V. V. Belykh, A. Y. Kuntsevich, M. M. Glazov, K. V. Kavokin, D. R. Yakovlev, and M. Bayer, Phys. Rev. X 8, 031021 (2018).
- [35] Y. Ohno, R. Terauchi, T. Adachi, F. Matsukura, and H. Ohno, Phys. Rev. Lett. **83**, 4196 (1999).
- [36] A. V. Kimel, F. Bentivegna, V. N. Gridnev, V. V. Pavlov, R. V. Pisarev, and Th. Rasing, Phys. Rev. B **63**, 235201 (2001).
- [37] P. E. Hohage, G. Bacher, D. Reuter, and A. D. Wieck, Appl. Phys. Lett. 89, 231101 (2006).
- [38] Z. G. Yu, S. Krishnamurthy, M. van Schilfgaarde, and N. Newman, Phys, Rev. B **71**, 245312 (2005).
- [39] M. D. Mower, G. Vignale, and I. V. Tokatly, Phys. Rev. B 83, 155205 (2011).
- [40] G. Marchetti, M. Hodgson, J. McHugh, R. Chantrell, and I. D'Amico, Materials 7, 2795 (2014).
- [41] P. Dey, L. Yang, C. Robert, G. Wang, B. Urbaszek, X. Marie, and S. A. Crooker, Phys. Rev. Lett. 119, 137401 (2017).
- [42] J. Li, M. Goryca, K. Yumigeta, H. Li, S. Tongay, and S. A. Crooker, Phys. Rev. Mater. 5, 044001 (2021).
- [43] Z. Gong, G. Liu, H. Yu, D. Xiao, X. Cui, X. Xu, and W. Yao, Nat. Commun. 4, 1 (2013).
- [44] X. Xu, W. Yao, D. Xiao, and T. F. Heinz, Nat. Phys. 10, 343 (2014).
- [45] H. Khani and S. P. Pishekloo, Nanoscale 12, 22281 (2020).

- [46] X. Song, S. Xie, K. Kang, J. Park, and V. Sih, Nano Lett. 16, 5010 (2016).
- [47] M. H. D. Guimaraes and B. Koopmans, Phys. Rev. Lett. 120, 266801 (2018).
- [48] J. Ye, Y. Li, T. Yan, G. Zhai, and X. Zhang, J. Phys. Chem. Lett. 10, 2963 (2019).
- [49] R. Bertoni, C. W. Nicholson, L. Waldecker, H. Hubener, C. Monney, U. De Giovannini, M. Puppin, M. Hoesch, E. Springate, R. T. Chapman, C. Cacho, M. Wolf, A. Rubio, and R. Ernstorfer, Phys. Rev. Lett. 117, 277201 (2016).
- [50] F. Rossi and T. Kuhn, Rev. Mod. Phys. 74, 895 (2002).
- [51] L. Yang, N. A. Sinitsyn, W. Chen, J. Yuan, J. Zhang, J. Lou, and S. A. Crooker, Nat. Phys. 11, 830 (2015).
- [52] R. C. Iotti and F. Rossi, Eur. Phys. J. B 90, 1 (2017).
- [53] F. Giustino, Rev. Mod. Phys. 89, 015003 (2017).
- [54] C. Jacoboni, Theory of Electron Transport in Semiconductors: A Pathway from Elementary Physics to Nonequilibrium Green Functions (Springer Science & Business Media, 2010), Vol. 165.
- [55] Y. Joly, *Interaction of Polarized Light with Matter*, edited by E. Beaurepaire, H. Bulou, F. Scheurer, and K. Jean-Paul, Magnetism and Synchrotron Radiation. Springer Proceedings in Physics, Vol. 133 (Springer, Berlin, Heidelberg, 2009).
- [56] M. D'Alessandro and D. Sangalli, Phys. Rev. B 102, 104437 (2020).
- [57] K. Hannewald, S. Glutsch, and F. Bechstedt, Phys. Rev. B 61, 10792 (2000).
- [58] A. Molina-Sánchez, D. Sangalli, L. Wirtz, and A. Marini, Nano Lett. 17, 4549 (2017).
- [59] N. Mainkar, D. A. Browne, and J. Callaway, Phys. Rev. B 53, 3692 (1996).
- [60] R. Sundararaman, K. Letchworth-Weaver, K. A. Schwarz, D. Gunceler, Y. Ozhabes, and T. A. Arias, SoftwareX 6, 278 (2017).
- [61] O. Madelung, U. Rosseler, and M. Schulz, Group IV Elements, IV-IV and III-V Compounds. Part A—Lattice Properties (Springer-Verlag, Berlin, 2001).
- [62] J. Sun, A. Ruzsinszky, and J. P. Perdew, Phys. Rev. Lett. **115**, 036402 (2015).
- [63] See Supplemental Material at http://link.aps.org/supplemental/ 10.1103/PhysRevB.104.184418 for electronic band structure, phonon dispersions, convergence tests, and the treatment of scattering processes for holes.
- [64] J. Tao, J. P. Perdew, V. N. Staroverov, and G. E. Scuseria, Phys. Rev. Lett. 91, 146401 (2003).
- [65] J. P. Perdew, K. Burke, and M. Ernzerhof, Phys. Rev. Lett. 77, 3865 (1996).
- [66] J. Sun, J. P. Perdew, and A. Ruzsinszky, Proc. Natl. Acad. Sci. USA 112, 685 (2015).
- [67] O. Madelung, Semiconductors (Springer, Berlin, 1987).
- [68] S. Grimme, J. Comput. Chem. 27, 1787 (2006).
- [69] M. K. Agarwal and P. A. Wani, Mater. Res. Bull. 14, 825 (1979).
- [70] D. R. Hamann, Phys. Rev. B 88, 085117 (2013).
- [71] N. Marzari and D. Vanderbilt, Phys. Rev. B **56**, 12847 (1997).
- [72] A. M. Brown, R. Sundararaman, P. Narang, W. A. Goddard, and H. A. Atwater, ACS Nano 10, 957 (2016).
- [73] P. Narang, L. Zhao, S. Claybrook, and R. Sundararaman, Adv. Opt. Mater. 5, 1600914 (2017).

- [74] A. M. Brown, R. Sundararaman, P. Narang, A. M. Schwartzberg, W. A. Goddard III, and H. A. Atwater, Phys. Rev. Lett. 118, 087401 (2017).
- [75] A. Habib, R. Florio, and R. Sundararaman, J. Opt. 20, 064001 (2018).
- [76] A. M. Brown, R. Sundararaman, P. Narang, W. A. Goddard III, and H. A. Atwater, Phys. Rev. B 94, 075120 (2016).
- [77] C. Verdi and F. Giustino, Phys. Rev. Lett. 115, 176401 (2015).
- [78] T. Sohier, M. Calandra, and F. Mauri, Phys. Rev. B 94, 085415 (2016).
- [79] T. Sohier, M. Gibertini, M. Calandra, F. Mauri, and N. Marzari, Nano Lett. 17, 3758 (2017).
- [80] P. Giannozzi, S. Baroni, N. Bonini, M. Calandra, R. Car, C. Cavazzoni, D. Ceresoli, G. L. Chiarotti, M. Cococcioni, I. Dabo *et al.*, J. Condens. Matter Phys. 21, 395502 (2009).
- [81] A. R. Bungay, S. V. Popov, I. R. Shatwell, and N. I. Zheludev, Phys. Lett. A 234, 379 (1997).
- [82] G. Dresselhaus, Phys. Rev. 100, 580 (1955).
- [83] M. Goryca, N. P. Wilson, P. Dey, X. Xu, and S. A. Crooker, Sci. Adv. 5, eaau4899 (2019).
- [84] T. Yan, S. Yang, D. Li, and X. Cui, Phys. Rev. B 95, 241406(R) (2017).
- [85] D. Wang, D. Han, D. West, N. Chen, S. Xie, W. Q. Tian, V. Meunier, S. Zhang, and X. Li, npj Comput. Mater. 5, 1 (2019).
- [86] D. Edelberg, D. Rhodes, A. Kerelsky, B. Kim, J. Wang, A. Zangiabadi, C. Kim, A. Abhinandan, J. Ardelean, M. Scully et al., Nano Lett. 19, 4371 (2019).

- [87] D. Rhodes, S. H. Chae, R. Ribeiro-Palau, and J. Hone, Nat. Mater. 18, 541 (2019).
- [88] M. Yankowitz, D. McKenzie, and B. J. LeRoy, Phys. Rev. Lett. 115, 136803 (2015).
- [89] H. G. Kim and H. J. Choi, Phys. Rev. B 103, 085404 (2021).
- [90] W. Zhao, R. M. Ribeiro, M. Toh, A. Carvalho, C. Kloc, A. H. Castro Neto, and G. Eda, Nano Lett. 13, 5627 (2013).
- [91] M. Palummo, M. Bernardi, and J. C. Grossman, Nano Lett. 15, 2794 (2015).
- [92] A. J. Goodman, A. P. Willard, and W. A. Tisdale, Phys. Rev. B 96, 121404(R) (2017).
- [93] J. Towns, T. Cockerill, M. Dahan, I. Foster, K. Gaither, A. Grimshaw, V. Hazlewood, S. Lathrop, D. Lifka, G. D. Peterson, R. Roskies, J. R. Scott, and N. Wilkins-Diehr, Comput. Sci. Eng. 16, 62 (2014).
- [94] R. Sundararaman and Y. Ping, J. Chem. Phys. 146, 104109 (2017).
- [95] P. I. Tamborenea, M. A. Kuroda, and F. L. Bottesi, Phys. Rev. B 68, 245205 (2003).
- [96] F. Aryasetiawan and S. Biermann, Phys. Rev. Lett. 100, 116402 (2008).
- [97] C. Grimaldi and P. Fulde, Phys. Rev. B 55, 15523 (1997).
- [98] X. Wu, D. Vanderbilt, and D. R. Hamann, Phys. Rev. B 72, 035105 (2005).
- [99] J. J. Zhou and M. Bernardi, Phys. Rev. B 94, 201201(R) (2016).
- [100] L. X. Benedict, C. D. Spataru, and S. G. Louie, Phys, Rev. B 66, 085116 (2002).